Langmuir Circulation in the Presence of Lateral Density Gradients

BY

Ke Li

B.E., University of Science and Technology of China (2007)

THESIS

Submitted to the University of New Hampshire
in partial fulfillment of
the requirements for the degree of

Master of Science

in

Mechanical Engineering

December 2010

This thesis has been examined and approved.

Thesis director, Gregory P. Chini

Associate Professor of Mechanical Engineering

Chris White

Assistant Professor of Mechanical Engineering

John McHugh

Associate Professor of Mechanical Engineering

Date

Acknowledgments

There are number of people without whom this thesis might not have been written, and to whom I am greatly indebted.

To my dearest girl friend Kristen Wallace and also to her family, her parents Mrs. & Mr. Wallace and her sister Kelly. They were very understanding, supportive and provided me with a very cozy environment at their house for me whenever I came back to New Hampshire to have meetings with my advisor. A sincere thank you to Mrs. and Mr. Wallace for your kind reminders on improving my research. I am also thankful to Kelly, who cheered me up with her clarinet and the movie Madagascar during the stressful thesis writing up time. Last but most honorably, I am grateful of Kristen for backing me up and helping me going through difficulty with a loving heart. Thanks you for being a wittiness of all the detailed and bumpy procedures of my thesis. Thank you for your emotional and practical support. With you gifted in my life, every steps are filled with joy!

To my landlord Mr. Dave Zelie and the house keeper, Mr. Philip Brogan together with other gentlemen of the Lighthouse Student Ministries. Thanks for welcoming this "random Chinese guy" into our brotherly community, where I spent most of my time and finished the majority of the writing. Also thanks for showing me a way of life filled with confidence and love. Never forgotten are those brothers who always gave me a hand, helping me to pick up myself from the places I stumbled in my life and strengthened my mind.

To my neighbor/best friends Mrs. Sandra & Mr. Franky Massie, a beautiful Indonesian couple who lived right above my room in the Lighthouse. Thanks for show me a great example of life all through my thesis writing. It is their who provided a great testimony of self-improving and optimism, which contributed a great deal to my academic life.

To my brothers and sisters in Christ of the UNH Campus Crusade and the Grad Inter-Varsity. In particular, I would like to give many thanks to Miss Iulia Barbu, a PhD student

Trust in the Lord with all your heart and lean not on your own understanding;

In all your ways acknowledge him,

And he will make your paths straight

—*Bible Prov 3:5,6*

Table of Contents

List of Figures

ABSTRACT

Langmuir Circulation in the Presence of Lateral Density Gradients

by

Ke Li

University of New Hampshire, December, 2010

Comparably little is known about the impact of lateral density gradients associated with, e.g., submesoscale fronts on Langmuir circulation in the ocean surface mixed layer. In this investigation, two-dimensional pseudospectral numerical simulations of the laterally stratified Craik–Leibovich (CL) equations are performed to elucidate the effect of an imposed horizontal density gradient on Langmuir cells. The dominant instability mode is found to consist of counter-rotating cells with up- and downwelling jets inclined to the vertical. Linear stability analysis confirms that, although no instability occurs in the absence of the CL vortex torque, the dominant instability mode exhibits growth rates exceeding those realized in a constant density fluid. An energy budget is used to gain insight into the physics of this cooperative instability. The fully nonlinear numerical simulations reveal a secondary instability, in which the tilted cells are laterally sheared, and a subsequent energy cascade to fine scales.

CHAPTER 1

INTRODUCTION
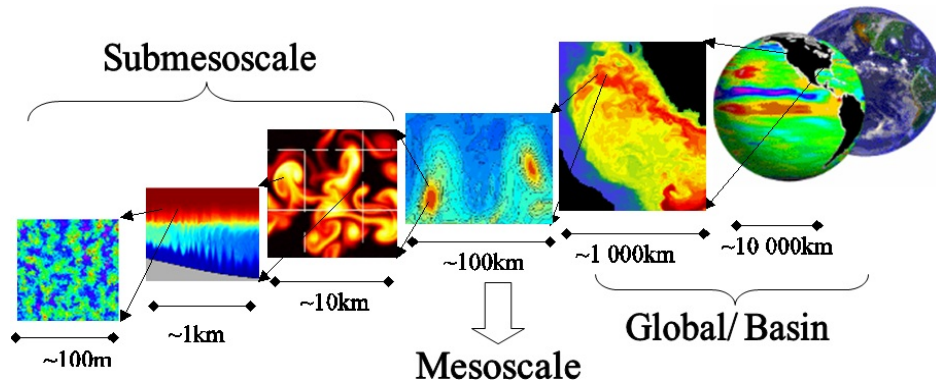
Figure 1-1: Spacial scale divisions of ocean dynamics, based on the characteristic length scale of oceanic motions. (Marshall, PAOC)

Geophysical Fluid Dynamics is the general genre of this article. It is a subject that applies fluid dynamics to oceanic and atmospheric motions, where planetary Coriolis force causes an extraordinary impact. This subject includes oceanography, meteorology, climate dynamics, ocean biology, and environmental science.

Parameterization is very important in oceanography area. Conception of spacial and temporal scales is employed to categorize various oceanic motions based on their characteristic sizes and durance. Shown in figure 1-1, large/basin scale ranges around

$1,000km \sim 10,000km$, at which the ocean's vertical structure can be approximated with hydrostatic balance when vertical acceleration of motion is very small compared with gravity. The motion is more influenced by the earth rotation. It keeps the pressure driven flow perpendicular to the pressure gradient (geostropic balance). Physical phenomena in this scales are meridional overturning circulation (MOC, also known as global conveyer belt), Antarctica Circumpolar Current (ACC). Mesoscale measures the oceanic motions that vary around $100km$, such as subtropical jets, subtropical large eddies. In this category, the dynamical balance gives the flow advected by a coriolis acceleration and pressure-gradient-driven flow (also known as geostrophic flow). Submesoscale provides a spacial scale of $100m \sim 10km$, where the ocean system is a combination of earth rotation, wind stress, viscous stress, boundary layers. The conventional motions in this category are subtropical baroclinic eddies, ocean carbon cycle, etc.

Ocean generally interacts with space through a thin layer, which is called mixed layer. In this layer, physical features of the ocean, such as temperature, salinity, density, and oxygen/carbon dioxide content, remain constant along depth due to the frequent mixing process, such as ocean turbulence driven by the wind, vertical thermal convection, surface cooling/warming associated with the solar radiation, or precipitations from the atmosphere.

Lateral density gradients associated with submesoscale fronts are ubiquitous in the ocean surface mixed layer (Boccaletti et al 2007). These fronts have a width on the order of one to ten kilometers and are nominally in gradient wind balance; i.e., the cross-front hydrostatic pressure gradient is balanced by Coriolis forces associated with a vertically sheared along-front current. There has been significant recent interest in understanding frontal instabilities and their role in the consequent restratification of the mixed layer [REFS]. However, less attention has been paid to the impact of lateral

density gradients on smaller scale convective (vertical) mixing processes that often act independently of the frontal dynamics. One notable exception is the recent study by Taylor and Ferrari 2010 of the impact of a geostrophically balanced lateral density gradient on turbulent convection in the upper ocean. Their results showed that the presence of the density front can modify the structure of the *vertical* stratification and the development of the surface boundary layer.

Like buoyancy driven convection, wind and surface-wave driven Langmuir circulation is a primary vertical mixing mechanism in the ocean surface boundary layer . Indeed, various numerical and observational studies have demonstrated that, under wind-forced seas, Langmuir cells dominate vertical transport and mixing in the upper ocean over depths up to $O(100)$ meters. Perhaps not surprisingly, the focus of nearly all systematic numerical process studies of Langmuir circulation in a density stratified environment – starting with a series of two-dimensional (downwind invariant) numerical simulations by Li and Garrett 1993, and continuing with fully three-dimensional large-eddy simulations (LES) of turbulent Langmuir circulation by (Thorpe 2004, McWilliams et al 2007, Leibovich 1977, Leibovich 1983) – has been on the effects of an imposed *vertically-varying* density profile on the development of the vortices and the evolution of the surface mixed layer.

Motivated by the routine occurrence of submesoscale fronts in the mixed layer, we here address a simple but complementary question: What is the influence of an *imposed lateral* density gradient on Langmuir circulation (LC)? Thus, we do not consider the possible two-way coupling between LC and the more slowly evolving submesoscale fronts – although we view the present investigation as a necessary first step toward addressing the multiscale interaction between fronts and mixed layer turbulence. Our primary aim is to elucidate the nature of the convective instability and the physical mechanisms involved. Thus, we consider an idealized scenario in

which the dynamics are two-dimensional (2D), with no variation in the along-front direction. We also imagine that the LC evolves in a preexisting mixed layer which is "slippery" to the cellular flow and has a sufficiently strong pyconcline to inhibit further deepening by the cells over the time scales of interest. Further details of the problem formulation are given in Chapter 2. Using a complement of linear stability theory, energy budgets, and fully nonlinear, non-hydrostatic numerical simulations of the laterally stratified 2D Craik–Leibovich (CL) equations (Chapter 3, Chapter 4, and Chapter 5, respectively), we diagnose the physics of the fastest growing primary instability mode and its subsequent secondary instability and nonlinear evolution. We conclude in Chapter 6 with a discussion of the implications of our results.

CHAPTER 2

Problem Formulation

As shown in Figure 2-1, we adopt a Cartesian coordinate system in which the x axis is aligned with the front and with the presumed direction of both the wind and the vertically-varying surface wave Stokes drift velocity $\mathbf{U_s} = U_s(z)\hat{\mathbf{x}}$. The vertical coordinate z measures distance upward from the mean position of the sea surface, and the cross-front coordinate y is oriented so as to complete a right-handed coordinate system. To explore the dynamics of LC and other phenomena characterized by time scales long compared to the typical surface wave period, we employ the CL equations – a surface-wave filtered version of the incompressible Navier–Stokes equations – under the Boussinesq approximation, *viz.*

$$\frac{\mathrm{D}\mathbf{U}}{\mathrm{D}t} \;\; = \;\; -\frac{1}{\rho_0}\nabla p \,-\, \frac{\rho}{\rho_0}g\hat{\mathbf{z}} \,+\, \mathbf{U_s} \times (\nabla \times \mathbf{U}) \,+\, \nu_e \nabla^2 \mathbf{U}. \tag{2.1}$$

Here, $\rho(x, y, z, t)$ is the density field, with ρ_0 a constant representative value; $\mathbf{U} = (U, V, W)$ is the velocity field; g is the gravitational acceleration; and ν_e is the presumed constant eddy viscosity that arises from the Craik–Leibovich wave filtering procedure. The substantial derivative operator $\mathrm{D}/\mathrm{D}t = \partial/\partial t + \mathbf{u} \cdot \nabla$, where t is the time variable. The third term on the right-hand side of (2.1) is the CL vortex force, the cross-product of the Stokes drift velocity associated with the filtered surface waves – a *prescribed* input in this formalism – and the (time or phase averaged) vorticity vector.
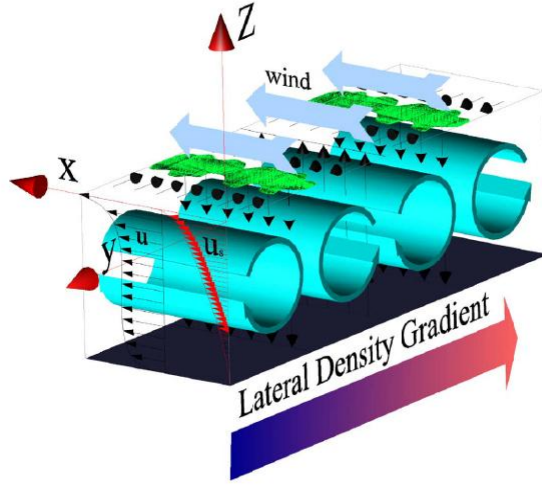
Figure 2-1: Schematic of LC roll vortices in the presence of a horizontal density gradient

Since individual Langmuir cells have $O(100)$ m cross-wind and vertical length scales, it is generally argued that Coriolis accelerations do not *directly* influence the dynamics of LC, although the Earth's rotation certainly influences the structure of submesoscale fronts. For simplicity, we do not include Coriolis accelerations in our analysis. Consequently, we choose not to explicitly incorporate those processes having larger space and longer time scales (and involving Coriolis accelerations) that are responsible for maintaining the front.

Numerous prior studies have shown that the dominant (i.e. fastest growing, most energetic) instability modes take the form of x invariant roll vortices, or "Langmuir cells," when the wind and waves are aligned in the x direction and Coriolis forces are neglected. We presume this to be the case even when lateral stratification is incorporated and henceforth restrict attention to x invariant dynamics (although we allow for flow in the x direction). To non-dimensionalize the governing equations, we

choose the mixed layer depth H to be the relevant length scale; $U_* \equiv u_* Re_*$ to be the downwind velocity scale, where $u_* = \sqrt{\tau_w/\rho_0}$ is the water friction velocity (and τ_w is the magnitude of the applied wind stress in the x direction) and the friction Reynolds number $Re_* = u_* H/\nu_e$; $W_* \equiv \sqrt{U_* U_{s0}}$ to be the cross-wind and the vertical velocity scale, where $U_{s0} = U_s(0)$; and the LC eddy turnover time H/V to be the time scale. Attributing density variations entirely to temperature gradients, and assuming a linear equation of state relating density ρ to the temperature T, we scale temperature anomalies by

$$\Delta T \equiv \frac{\mathrm{d}T_f}{\mathrm{d}y} H \equiv \left(\frac{1}{\alpha g} M^2\right) H, \tag{2.2}$$

roughly the temperature difference across a typical Langmuir cell. In (2.2), $T_f(y)$ is the imposed, *linear* lateral stratification (with constant gradient $\mathrm{d}T_f/\mathrm{d}y$ and T_0 the reference temperature corresponding to ρ_0), α is the coefficient of thermal expansion of seawater, and M is, thus, the Brunt frequency associated with the horizontal density gradient.

Using these scalings, the non-dimensional laterally stratified CL equations can be cast in a stream-function/vorticity form:

$$U_t + \Psi_z U_y - \Psi_y U_z = La \nabla^2 U, \tag{2.3}$$

$$\Omega_t + \Psi_z \Omega_y - \Psi_y \Omega_z = \frac{\mathrm{d}U_s}{\mathrm{d}z} U_y - Ri_h \Theta_y - \chi Ri_h + La \nabla^2 \Omega, \tag{2.4}$$

$$\nabla^2 \Psi = \Omega, \tag{2.5}$$

$$\Theta_t + \Psi_z \Theta_y - \Psi_y \Theta_z = -\Psi_z + Pe^{-1} \nabla^2 \Theta. \tag{2.6}$$

In (2.3)–(2.6), all variables are now non-dimensional and subscripts denote partial differentiation. The (non-dimensional) total temperature field has been decomposed into the imposed background plus a deviation, i.e.

$$T(y, z, t) = y + \Theta(y, z, t).$$

Ω is the negative of the x vorticity component and Ψ is the associated stream function, with $V = \Psi_z$ and $W = -\Psi_y$. For analytical simplicity, we take the Stokes drift to be a linear rather than more realistic exponentially-decaying function of depth, $U_s(z) = z + 1$, but qualitatively similar results are likely to be obtained with any monotonically decaying profile. Three non-dimensional parameters appear in these equations: the laminar Langmuir number $La \equiv \nu_e/(W_*H)$, which can be interpreted as an inverse Reynolds number based on the vertical velocity scale; the Peclet number $Pe \equiv W_*H/\kappa_e$, where κ_e is an eddy diffusivity for heat; and the *horizontal* Richardson number $Ri_h \equiv M^2/(W_*/H)^2$.

The parameter χ is either zero or unity enabling us to model two qualitatively different scenarios within the same mathematical and computational framework. When $\chi = 1$, hydrostatic pressure variations induced by the imposed lateral density gradient drive a cross-frontal shear flow $V^b(z)$. This lateral shear flow advects the temperature field, creating *vertical* density gradients:

$$T(y,z,t) = y + \Theta^b(z) + \theta(y,z,t), \tag{2.7}$$

where the steady base temperature field $y + \Theta^b(z)$ is 2D and $\theta(y,z,t)$ measures departures from this basic state. Although the $\chi = 1$ scenario, henceforth referred to as the "free" case, yields a cleanly posed mathematical and physical problem, its oceanographic relevance is somewhat suspect because the pressure-driven lateral shear flow is balanced by vertical *diffusion* of y momentum. As noted in § **??**, we are motivated by the occurrence of submesoscale fronts in the mixed layer. In this case, a better conceptual model is that the front is in thermal wind balance in which the vertically-varying lateral pressure gradient (induced by the density gradient) drives an equilibrium *along-front* flow – owing to Coriolis accelerations – that also is vertically sheared, i.e. with *no* cross-frontal shear flow. Although we neglect Coriolis accelerations in this investigation, we can nevertheless model this situation, in which

8

the lateral density gradient is "frozen" in place without driving a lateral shear flow, simply by setting the switching parameter $\chi = 0$ and acknowledging that the *wind-driven* along-front shear flow would be modified by the "thermal wind" in this case, an effect that we do not explicitly attempt to capture. We conveniently treat both the free and the frozen cases below within a single framework by setting $\chi = 1$ and $\chi = 0$, respectively.

To complete the problem specification, (2.3)–(2.6) are supplemented by the following dimensionless boundary conditions at the mean position of the free surface $z = 0$ and along the mixed layer base $z = -1$:

$$U_z = 1, \qquad \Omega = 0, \qquad \Psi = 0, \qquad \Theta_z = 0. \tag{2.8}$$

All fields are taken to be L-periodic in the y coordinate, where L is the non-dimensional "width" of the front.

In what follows, we fix La and Pe at moderately small and large values, respectively, and treat Ri_h, which measures the strength of the imposed lateral stratification relative to the cellular shear, as the key control parameter.

CHAPTER 3

Linear Stability Analysis

3.1 Derivation

To gain insight into the convective structures likely to emerge from the base state described in § ??, we first perform a linear stability analysis. Each generic dependent variable Φ is decomposed into a steady base state contribution (denoted with a superscript "b") and a small amplitude perturbation (denoted with lowercase variables):

$$\Phi(y, z, t) \;=\; \Phi^b(z) \;+\; \phi(y, z, t). \tag{3.1}$$

The basic state fields are readily found to be

$$U^b = z + 1, \tag{3.2}$$

$$\Omega^b = \chi \cdot \frac{Ri_h}{2La} \left(z^2 + z \right), \tag{3.3}$$

$$\Psi^b = \chi \cdot \frac{Ri_h}{24La} \left(z^4 + 2z^3 - z \right), \tag{3.4}$$

$$\Theta^b = \chi \cdot \frac{PeRi_h}{24La} \left(\frac{1}{5} z^5 + \frac{1}{2} z^4 - \frac{1}{2} z^2 \right). \tag{3.5}$$

These are plotted in Figure 3-7 for $\chi = 1$. When $\chi = 0$, the only non-zero base state field is $U^b(z)$. Substituting the decomposition (3.1) into (2.3)–(2.6) and linearizing yields the equations governing the perturbation fields:

$$u_t + \Psi_z^b u_y - \psi_y U_z^b = La(u_{yy} + u_{zz}), \tag{3.6}$$

$$\omega_t + \Psi_z^b \omega_y - \psi_y \Omega_z^b = \frac{\mathrm{d}U_s}{\mathrm{d}z} u_y - Ri_h \theta_y + La(\omega_{yy} + \omega_{zz}), \tag{3.7}$$

$$\theta_t + \Psi_z^b \theta_y - \psi_y \Theta_z^b = -\psi_z + Pe^{-1}(\theta_{yy} + \theta_{zz}), \tag{3.8}$$

$$\nabla^2 \psi = \omega. \tag{3.9}$$

The perturbation fields are L periodic in the y coordinate and satisfy homogeneous boundary conditions along $z = 0$ and $z = -1$:

$$u_z = 0, \qquad \omega = 0, \qquad \psi = 0, \qquad \theta_z = 0. \tag{3.10}$$

Decomposing the generic perturbation field

$$\phi(y, z, t) = \phi_0(z)e^{iky}e^{\sigma t} + c.c. \tag{3.11}$$

yields an ordinary differential eigenvalue problem in z for each horizontal wavenumber k, where $\phi_0(z)$ and σ are the (generally complex) vertical eigenfunction and eigenvalue. We solve this problem using a Chebyshev spectral collocation method with 20–40 modes.

3.2 Chebyshev Spectral Collocation Method

Known for its high precision, spectral method is a general computational method, widely applied in mathematics and scientific computing, for solving partial differential equations (PDEs) and ordinary differential equations (ODEs). Often it involves Fast Fourier transform (FFT) as the main foundation. Solutions under this method are broken down into linear combinations of a series of nonzero function sets, eg sinusoids in FFT and polynomials in Chebyshev transform. Each of the function sets covers the whole domain. Chebyshev spectral collocation methods is an implicit computational spectral method, which enables boundary conditions of different types, eg. Neumann or Direchlet conditions, to be added to equation systems. Solutions are linear combinations of Chebyshev series. The virtue of this method is its high precision and non periodic domain requirement. Based on Chebyshev series, a Chebyshev

$$D_N = \begin{bmatrix} \dfrac{2N^2+1}{6} & 2\dfrac{(-1)^j}{1-x_j} & \dfrac{1}{2}(-1)^N \\[2ex] -\dfrac{1}{2}\dfrac{(-1)^i}{1-x_i} & \dfrac{(-1)^{i+j}}{x_i-x_j} \quad \dfrac{-x_j}{2(1-x_j^2)} \quad \dfrac{(-1)^{i+j}}{x_i-x_j} & \dfrac{1}{2}\dfrac{(-1)^{N+i}}{1+x_i} \\[2ex] -\dfrac{1}{2}(-1)^N & -2\dfrac{(-1)^{N+j}}{1+x_j} & -\dfrac{2N^2+1}{6} \end{bmatrix}$$

Figure 3-1: Differentiation matrix D_N of Chebyshev transform, over a domain of $(-1,1)$. Its size is $(N+1) \times (N+1)$, where $N+1$ is the domain resolution of the Chebyshev domain. $i \neq j$, and $i, j = 1, 2, ..., N-1$. (Spectral Methods in Matlab, Trefethen)

differentiation matrix D_N is defined as the descritized form of derivative.

$$\frac{d\phi_0(Z)}{dZ} \rightarrow D_N \cdot \phi_0(Z_i) \tag{3.12}$$

In this equation, $Z \in (-1,1)$ is the coordinates in which Chebyshev series are mathematically defined. $Z_i = \cos(\pi \cdot i/N)$, where N is the resolution and $N+1$ is the number of grid points in Z domain.

$$(D_N)_{00} = \frac{2N^2+1}{6} \tag{3.13}$$

$$(D_N)_{NN} = -\frac{2N^2+1}{6} \tag{3.14}$$

$$(D_N)_{jj} = -\frac{x_j}{2(1-x_j^2)} \qquad j = 1, ..., N-1 \tag{3.15}$$

$$(D_N)_{ij} = \frac{c_i}{c_j}\frac{(-1)^{i+j}}{x_i - x_j} \qquad i \neq j; i, j = 1, ..., N-1 \tag{3.16}$$

12

$$c_i = \begin{cases} 2 & i = 0 \text{ or } N \\ 1 & \text{otherwise} \end{cases}$$

In Matlab, a Chebyshev based differentiation matrix D_N is formed (see Figure 3-1) according to the definition. It transforms the differentiation operation into matrix multiplication, calculating derivatives along $Z \in (-1, 1)$ domain. In the simulation system $z \in -1, 0$. Define converting ratio $\xi = 2.0$ as $Z = \xi z + 1$. Therefore,

$$\frac{\partial \phi}{\partial z} = \xi \frac{\partial \phi}{\partial Z} = \xi D_N \phi \tag{3.17}$$

Substitute the field decomposition form, (Equation 3.11) in to the linearized perturbation equations (3.6) - (3.9). They turn out to be:

u-equation:

$$\sigma u_0 = [La(\xi^2 D_N^2 - k^2) - ik\Psi_z^b] \cdot u_0 + ikU_z^b \cdot \psi_0 \tag{3.18}$$

ω-equation

$$\sigma \omega_0 = [La(\xi^2 D_N^2 - k^2) - ik\Psi_z^b]\omega_0 + ik\Omega_z^b \cdot \psi_0 - ikRi_h \cdot \theta_0 + ik[u_s]_z \cdot u_0 \tag{3.19}$$

ψ-equation

$$0 = (\xi^2 D_N^2 - k^2) \cdot \psi_0 - \omega_0 \tag{3.20}$$

θ-equation

$$\sigma \theta_0 = [Pe^{-1}(\xi^2 D_N^2 - k^2) - ik\Psi_z^b] \cdot \theta_0 + [ik\Theta_z^b - \xi D_N] \cdot \psi_0 \tag{3.21}$$

In the equations, time changing rate θ and its corresponding vertical structure $\phi_0(z)$ as functions of horizontal wave number k are expected as eigenvalue and eigenfunction of the linear system. Rewrite the equations into the form of matrices.

$$\begin{pmatrix} A_{11} & A_{12} & A_{13} & A_{14} \\ A_{21} & A_{22} & A_{23} & A_{24} \\ A_{31} & A_{32} & A_{33} & A_{34} \\ A_{41} & A_{42} & A_{43} & A_{44} \end{pmatrix} \begin{pmatrix} u_0 \\ \omega_0 \\ \psi_0 \\ \theta_0 \end{pmatrix} = \sigma \begin{pmatrix} B_{11} & B_{12} & B_{13} & B_{14} \\ B_{21} & B_{22} & B_{23} & B_{24} \\ B_{31} & B_{32} & B_{33} & B_{34} \\ B_{41} & B_{42} & B_{43} & B_{44} \end{pmatrix} \begin{pmatrix} u_0 \\ \omega_0 \\ \psi_0 \\ \theta_0 \end{pmatrix}$$

$$[A] \qquad \phi_0 \qquad = \sigma \qquad [B] \qquad \phi_0$$

In matrix A, every elements are:

$$A_{11} = L_a(\xi^2 D_N^2 - k^2 I) - ik\Psi_z^b \qquad A_{12} = 0 \qquad A_{13} = ikU_z^b \qquad A_{14} = 0$$

$$A_{21} = ik[u_s]_z \qquad A_{22} = L_a(\xi^2 D_N^2 - k^2 I) - ik\Psi_z^b \qquad A_{23} = ik\Omega_z^b \qquad A_{24} = -ikRi_h \cdot I$$

$$A_{31} = 0 \qquad A_{32} = -I \qquad A_{33} = \xi^2 D_N^2 - k^2 I \qquad A_{34} = 0$$

$$A_{41} = 0 \qquad A_{42} = 0 \qquad A_{43} = ik\Theta_z^b - \xi D_N \qquad A_{44} = Pe^{-1}(\xi^2 D_N^2 - k^2 I) - ik\Psi_z^b$$

In matrix B, every elements are:

$$B_{11} = I \qquad B_{12} = 0 \qquad B_{13} = 0 \qquad B_{14} = 0$$

$$B_{21} = 0 \qquad B_{22} = I \qquad B_{23} = 0 \qquad B_{24} = 0$$

$$B_{31} = 0 \qquad B_{32} = 0 \qquad B_{33} = 0 \qquad B_{34} = 0$$

$$B_{41} = 0 \qquad B_{42} = 0 \qquad B_{43} = 0 \qquad B_{44} = I$$

where each one's size is $(N+1) \times (N+1)$. I here refers to identical matrix. 0 refers to zero matrix. Figure(3-2a) shows the clear structure of the ordinary differential equations (ODEs) in the matrices' form. For boundary conditions, Direchlet and Neuman conditions are imposed differently. Direchlet boundary conditions in the linear system are illustrated in the form of $\phi_0(1) = \phi_0(N+1) = 0$. Variables in this category are ω_0 and ψ_0. As is shown in Figure(3-2b), four columns are eliminated because from left-land side, those columns are multiplied by 0 all the time, there are no contribution of them. Four rows get deleted because from right-hand sight, four boundaries' values in the vector ϕ_0 have been dropped off. Neuman boundary conditions in the linear system are denoted in the form of $\partial\phi_0/\partial z|_{z=-1,0} = 0$. The discretized condition is written into Chebyshev differentiation matrix form $D_N\phi_{0i}|_{i=1,N+1} = 0$. Below in the

14

matrix equation, $N = 6$ is set as an example.

$$
\begin{pmatrix}
\otimes & \otimes & \otimes & \otimes & \otimes & \otimes & \otimes \\
& ... & & & ... & & \\
& ... & & & ... & & \\
& ... & & & ... & & \\
& ... & & & ... & & \\
& ... & & & ... & & \\
\otimes & \otimes & \otimes & \otimes & \otimes & \otimes & \otimes
\end{pmatrix}
\begin{pmatrix}
\phi_{01} \\
\phi_{02} \\
\phi_{03} \\
\phi_{04} \\
\phi_{05} \\
\phi_{06} \\
\phi_{07}
\end{pmatrix}
=
\begin{pmatrix}
0 \\
. \\
. \\
. \\
. \\
. \\
0
\end{pmatrix}
$$

From the matrix multiplication, only the first row ($i = 1$) and last row ($i = N + 1$) determine the boundary conditions. As shown in Figure 3-2c, Neuman boundaries can be imposed by replacing the first and last row of the matrix operator with the ones on the differentiation matrix (see Figure 3-2c).

3.3 $\chi = 1$

The first important observation (confirmed by numerical solution of the eigenvalue problem) is that, for the free case ($\chi = 1$), *no* 2D linear instability is possible in the absence of surface wave effects. Indeed, if the Stokes drift (gradient) vanishes, then the downwind vorticity decouples from the downwind velocity; see (3.6) and (3.7); thus, convective flows generated in the cross-wind plane cannot benefit from production of disturbance energy by the downwind Reynolds stress component $< uw >$, where the angle brackets refer to a y–z spatial average. Moreover, direct calculation shows that the gradient Richardson number associated with the base state shear flow $V^b(z)$ in the cross-wind direction,

$$
Ri_g(z) \equiv Ri_h \frac{\mathrm{d}\Theta^b/\mathrm{d}z}{(\mathrm{d}V^b/\mathrm{d}z)^2},
$$

15

is given by

$$Ri_g(z) \;=\; \frac{PeLa}{6}\left(\frac{z^4 + 2z^3 - z}{z^4 + 2z^3 + z^2}\right).$$

The minimum value $Ri_{g_{min}} = (5/6)PeLa$. Hence, for $Pe \geq 3/(10La)$, the base state does not exhibit (Kelvin–Helmholtz) instabilities. This assertion is corroborated by the results shown in Figure 3-7, in which the real part of σ is plotted as a function of horizontal wavenumber in the free case for fixed values of La and Pe and various values of Ri_h. When surface wave effects are included, $\mathrm{d}U_s/\mathrm{d}z = 1$, and two distinct modes of instability are possible: (i) a stationary mode comprised of Langmuir cells inclined to the vertical (see Figure 3-3a); and (ii) traveling modes in which counter-rotating cells with vorticity maxima near the surface propagate in the direction of the background *density* gradient (see Figure 3-3b) and those with vorticity maxima near the mixed layer base propagate oppositely. The physics of these traveling-wave modes is described in more detail below.

3.4 $\chi = 0$

When the background density gradient is frozen (i.e. $\chi = 0$), gravitational instability *is* possible even in the absence of the CL vortex torque. As shown in figure 3-3bc, potential energy can be released (i.e. positive buoyancy production $\int w\theta dydz$) when counter-rotating convection cells are generated with up- and downwelling zones inclined in the direction of the density gradient. This geometrical configuration is readily understood by considering a parcel of fluid at mid-depth. When the parcel is displaced in the direction of decreasing density (i.e. increasing temperature) gradient – in the positive y direction – it finds itself heavier than the surrounding fluid at the same depth and, hence, has a tendency to sink. Conversely, when displaced in the opposite direction, the same parcel would tend to rise under the influence of

16

positive buoyancy. The growth rate versus wavenumber curves in Figure 3-4 confirm the existence of this convective instability. However, for typical submesoscale fronts, $Ri_h = O(0.1)$, and this purely gravitational instability is very weak, exhibiting growth rates $\sigma_r \leq 0.1$. For a ten-fold increase in the amplitude of an initial disturbance, roughly 40 time units is required or, in dimensional terms, approximately $O(20)$ hours. Over this duration, Coriolis effects would be expected to modify the purely gravitational instability into a phenomenon termed "slantwise convection" . In contrast, when surface wave effects are included, Langmuir cells are excited with growth rates a factor of 5 to 10 larger, as also shown in Figure 3-4. (In fact, even larger growth rates are obtained for smaller values of La.) Of course, the structure of the cells and the nature of the instability is modified to a greater or lesser extent depending upon the strength of the lateral density gradient. For example, at $Ri_h = 0.1$ and $La = 0.01$, the maximum growth rate is only slightly larger than that at $Ri_h = 0$ and the same value of La. However, in the former case, the eigenfunctions exhibit the expected tilt in the direction of increasing density. For a stronger front having $Ri_h = 1$, the maximum growth rate is increased by roughly 20% over that realized in the absence of lateral stratification, the cells are strongly inclined to the vertical (see Figure 3-5), and the aspect-ratio π/k of the fastest growing cells is notably smaller (i.e. leading to narrower cells) than is observed without stratification. Thus, for sufficiently strong fronts, buoyancy torques and CL vortex torque cooperate to yield enhanced growth rates relative to those realized when either instability mechanism operates in the absence of the other.

3.5 Analytical Prediction of Cell Tilt Angle

To gain further insight into the cell tilting phenomenon, we next perform an approximate but purely analytical stability analysis. To make the analysis tractable, we

neglect both viscous and thermal dissipative effects and, more significantly, we ignore the influence of the boundaries at $z = 0$ and $z = -1$ by assuming the dynamics to be vertically periodic. With these approximations, the linearized equations for the perturbations (3.6)–(3.9) can, for the frozen stratification scenario ($\chi = 0$), be reduced to a single equation for the stream function:

$$\nabla^2 \psi_{tt} - S\psi_{yy} - Ri_h\psi_{yz} \;\; = \;\; 0, \tag{3.22}$$

where S is zero or unity depending upon whether surface wave effects are included. Substituting $\psi = \psi_0 exp[i(ky + mz)]exp(\sigma t) + c.c$ yields

$$\sigma^2 \;\; = \;\; \frac{S\lambda^2 - Ri_h\lambda}{1 + \lambda^2}, \tag{3.23}$$

where $\lambda = -k/m$, the slope of tilt angle of a single Fourier mode. Thus, the eigenvalues are either purely real or purely imaginary, depending whether $S > Ri_h/|\lambda|$ or $S < Ri_h/|\lambda|$, respectively, for $\lambda > 0$ (and $Ri_h > 0$), while for $\lambda < 0$, the eigenvalues are strictly real. The value λ_m of λ which maximizes the magnitude of the growth rate is given by

$$\lambda_m \;\; = \;\; \frac{-S \overset{+}{-} \sqrt{S^2 + Ri_h^2}}{Ri_h}.$$

For $S = 0$, $|\lambda_m| = 1$. When $\lambda_m = -1$, buoyancy driven instability occurs, with $\sigma = \sqrt{Ri_h/2}$ for the fastest growing cells, which are inclined at an angle of 45 degrees to the vertical in the direction of increasing density gradient. When $\lambda = +1$, an oscillatory motion is obtained – this is essentially an *internal gravity wave* with frequency $\sqrt{Ri/2}$ and lines of constant phase inclined at 45 degrees to the vertical in the direction of *decreasing* density gradient. Thus, fluid parcels can oscillate under the influence of buoyancy anomalies in the presence of the lateral density gradient. When $S = 1$, the slope λ. In the y–z plane of the up- and downwelling zones of the fastest growing Langmuir cells is predicted to be

$$\lambda_m \;\; = \;\; \frac{-1 - \sqrt{1 + Ri_h^2}}{Ri_h}.$$

The implied tilt angle agrees very well with that observed in the eigenfunction plots obtained from the full linear stability problem; for example, see the solid line for $Ri_h = 4$ in Figure 3-5.
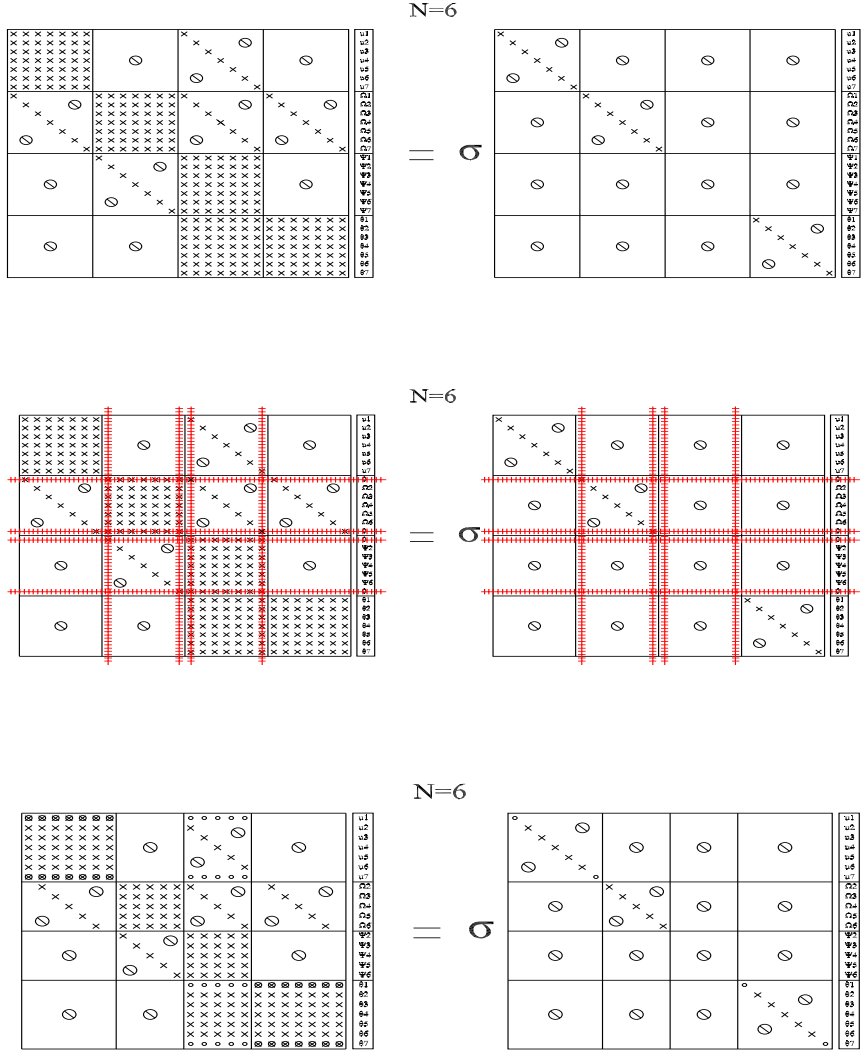
Figure 3-2: ODEs for an eigenvalue and eigenfunction problem, demonstrating the structure of matrices. Resolution is chosen to be $N = 6$. The matrices are written out with: (a)no boundary conditions ; (b)imposed Direchlet boundary conditions, by crossing out the rows and columns under the red lines; (c)imposed Neuman boundary conditions.
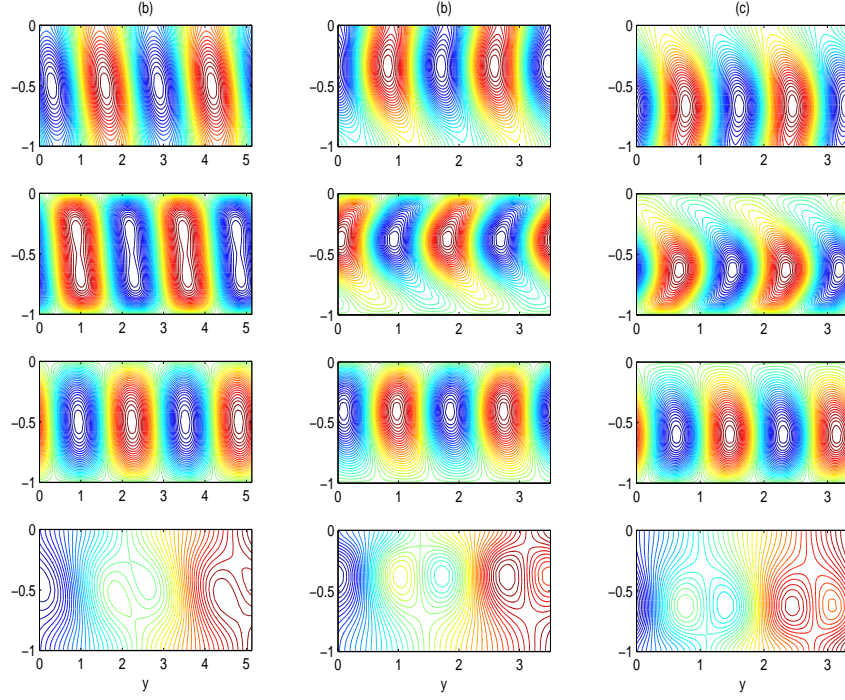
Figure 3-3: Linear theory results, the variables plotted are U, Ω, Ψ, T from top to the bottom: (a) Stationary mode eigenfunctions for $\chi = 1$, $La = 0.01$, $Pe = 4000$, and $Ri_h = 0.011$. The wavenumber $k = 2.44$, corresponding to the fastest-growing mode for these parameter values; (b) Leftward-propogating mode eigenfunctions for $\chi = 1$, $La = 0.01$, $Pe = 4000$, and $Ri_h = 0.016$. The wavenumber k =3.6; (c) Rightward-propogating mode eigenfunctions for $\chi = 1$, $La = 0.01$, $Pe = 4000$, and $Ri_h = 0.016$. The wavenumber $k = 3.7$.
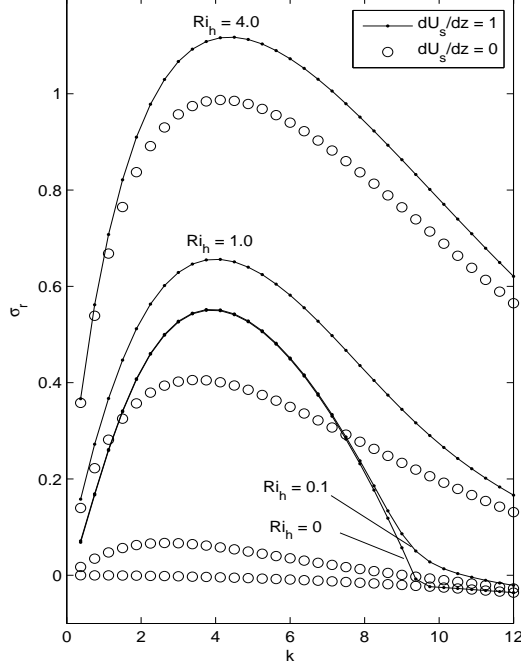
Figure 3-4: Maximum (strictly) real growth rate, σ_r, as a function of horizontal wavenumber k for the frozen case ($\chi = 0$) for $La = 0.01$, $Pe = 4000$, and $Ri_h = 0$, 0.01, 0.1, 1, 4. The dotted curves correspond to a scenario in which surface wave effects are absent, $dU_s/dz = 0$; linear instability is possible in this case, taking the form of tilted buoyancy-driven convection. The solid curves correspond to the case in which $dU_s/dz = 1$. Note that growth rates are much larger when surface wave effects are incorporated.
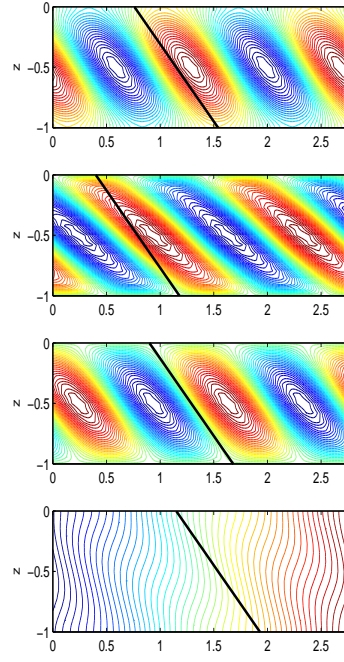
Figure 3-5: Stationary mode eigenfunctions for $\chi = 0$, $La = 0.01$, $Pe = 4000$, and $Ri_h = 4$. The wavenumber $k = 4.3$, the variables plotted are U, Ω, Ψ, T from top to the bottom
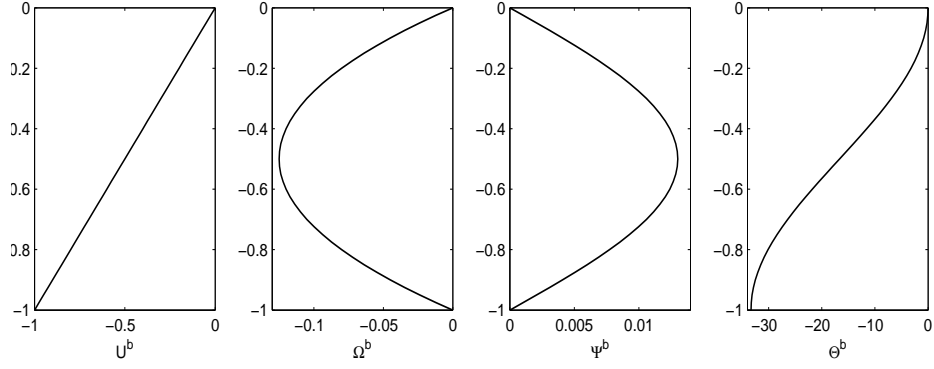
Figure 3-6: Base state fields for $La = 0.01$, $Pe = 4000$, $Ri_h = 0.01$, and $\chi = 1$ ("free case"). From left to right: along-front velocity $U^b(z)$, along-front vorticity $\Omega^b(z)$, cross-front stream function $\Psi^b(z)$, and *vertical* temperature profile $\Theta^b(z)$. For the "frozen" case, $\chi = 0$, the only non-zero basic state field is $U^b(z)$.
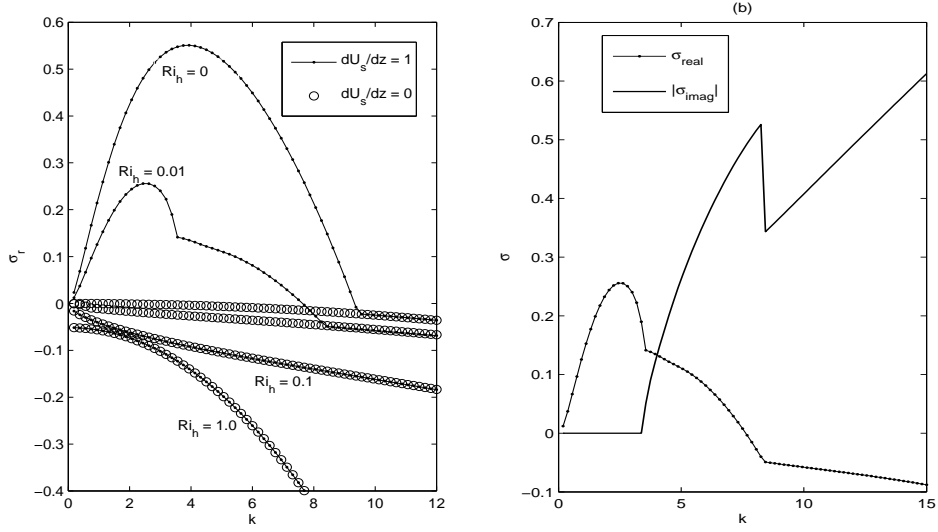
Figure 3-7: Maximum real part of the growth rate, σ_r, as a function of horizontal wavenumber k for the free case ($\chi = 1$) for $La = 0.01$, $Pe = 4000$, and $Ri_h = 0$, 0.01, 0.1, 1. The dotted curves correspond to a scenario in which surface wave effects are absent, $dU_s/dz = 0$; note there are no linear instabilities in this case. The solid curves correspond to the case in which $dU_s/dz = 1$, and instability is possible.
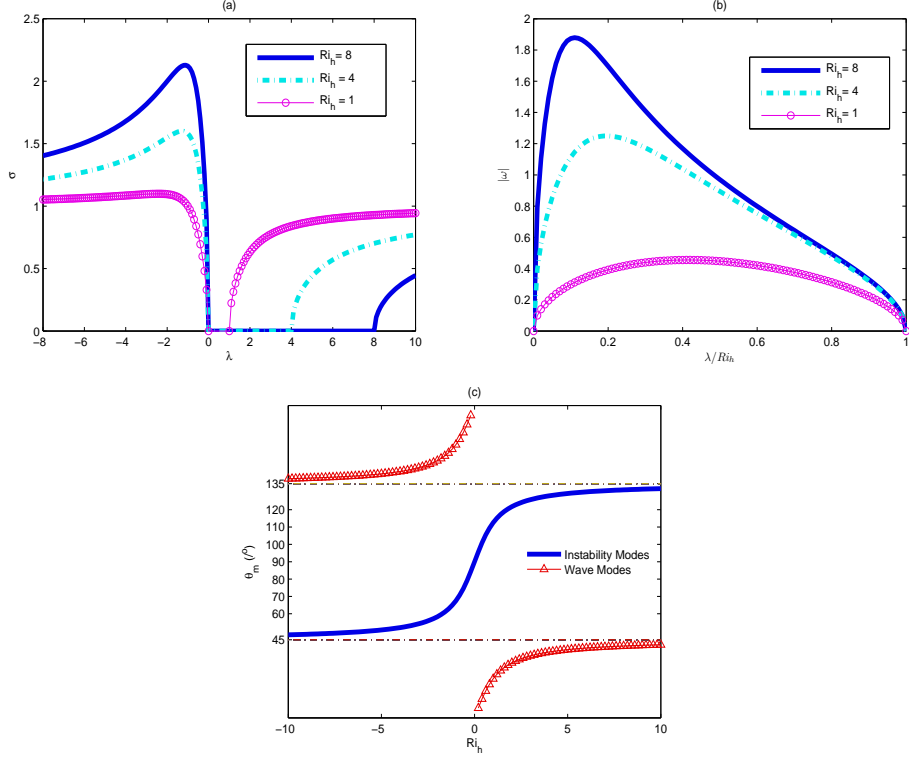
Figure 3-8: Maximum growth rate σ, as a function of modes' slopes s_m for the frozen case ($\chi = 0$) with assuming $La, Pe^{-1} \ll 1$: (a)Instability modes: growth rate σ varies with cells tilt angle for different Ri_h values. It shows the asymmetry of The plots illustrates the relation between eigenvalue sigma and modes slope s_m with different values of Ri_h; (b)wave modes: frequency varies with tilt angles for different Ri_h values; (c)The tilt angle from the horizontal line, at the direction of which a mode has the maximum growth rate in instability solutions or largest frequency in wave ones.

CHAPTER 4

Energy Budget
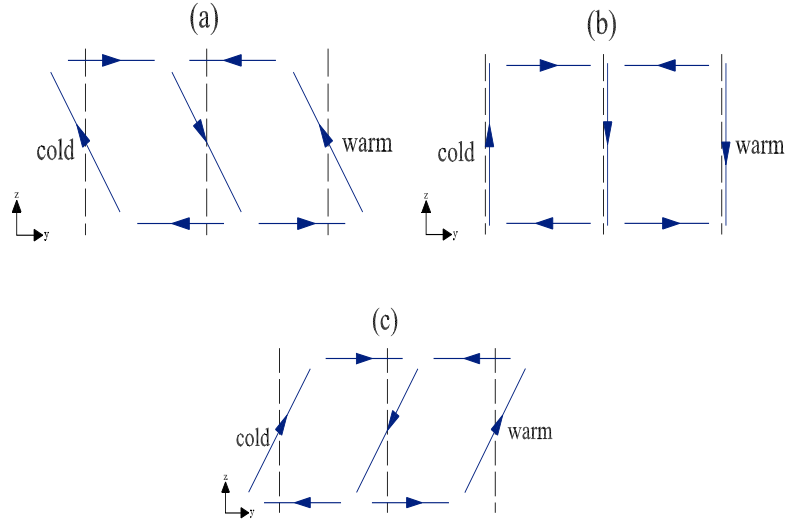
Figure 4-1: Schematic of cells tilting related with energy transport in the frozen background cases, the dotted lines are isopycnals the solid lines with arrows represent the cellular flow: (a). Kinetic energy transported to potential energy, $Ri_h \int w\theta > 0$; (b). No energy transport, $Ri_h \int w\theta = 0$; (c). Potential energy transported to kinetic energy, $Ri_h \int w\theta < 0$

We next examine the energetics of this system both to gain a better understanding of the energy transfers driving (or retarding) the primary instability as well as to aid

in the interpretation of the direct numerical simulations (DNS) described in the next section.

4.1 Derivation

To derive the energy budget, we substitute (3.1) into the governing (x-invariant) equations in primitive variables, yielding the following *exact* system:

$$\frac{D'u}{Dt} = La\nabla^2 u - (V^b\frac{\partial u}{\partial y} + w\frac{dU^b}{dz}), \tag{4.1}$$

$$\frac{D'v}{Dt} = -\frac{\partial \pi}{\partial y} + U_s\frac{\partial u}{\partial y} + La\nabla^2 v - (V^b\frac{\partial v}{\partial y} + w\frac{dV^b}{dz}), \tag{4.2}$$

$$\frac{D'w}{Dt} = -\frac{\partial \pi}{\partial z} + U_s\frac{\partial u}{\partial z} + La\nabla^2 w + Ri_h\theta - V^b\frac{\partial w}{\partial y}, \tag{4.3}$$

$$\frac{D'\theta}{Dt} = Pe^{-1}\nabla^2\theta - v - (V^b\frac{\partial \theta}{\partial y} + w\frac{d\Theta^b}{dz}), \tag{4.4}$$

$$\frac{\partial v}{\partial y} + \frac{\partial w}{\partial z} = 0, \tag{4.5}$$

where the operator $D'/Dt \equiv \partial/\partial t + v\,\partial/\partial y + w\,\partial/\partial z$ and π is the perturbation pressure.

The equation governing the evolution of the downwind perturbation kinetic energy (per unit mass),

$$KE'_{||} \equiv \ <(1/2)u^2>,$$

where

$$<(\cdot)> \ \equiv \ \frac{1}{L}\int_{-1}^{0}\int_{0}^{L}(\cdot)dydz$$

and $L = 2\pi/k$ is the width of the domain, is obtained by multiplying (4.1) by u and integrating over the domain:

$$\frac{dKE'_{||}}{dt} \ = \ P_U - D'_{||}, \tag{4.6}$$

where $P_U = - < uw\mathrm{d}U^b/\mathrm{d}z >$ accounts for the production of $KE'_\parallel$ by the downwind Reynolds stress, and $D'_\parallel = La < |\nabla u|^2 >$ is the viscous dissipation of $KE'_\parallel$. Proceeding in a similar fashion, the evolution of the cross-wind perturbation kinetic energy (per unit mass),

$$KE'_\perp \equiv < (1/2)(v^2 + w^2) >$$

is obtained by multiplying (4.2) by v and (4.3) by w and integrating over the domain, yielding

$$\frac{\mathrm{d}KE'_\perp}{\mathrm{d}t} = P_V + P_S + B - D'_\perp. \tag{4.7}$$

For convenience, the various terms in the energy equations are defined and tabulated below.

$-D_\parallel$	$-La < |\nabla u|^2 >$	dissipation of $KE'_\parallel$
$-D_\perp$	$-La < |\nabla v|^2 + |\nabla w|^2 >$	dissipation of $KE'_\perp$
B	$+Ri_h < w\theta >$	buoyancy production
P_S	$- < uw\frac{\mathrm{d}U_s}{\mathrm{d}z} >$	Stokes production
P_U	$- < uw\frac{\mathrm{d}U^b}{\mathrm{d}z} >$	x-shear production
P_V	$- < vw\frac{\mathrm{d}V^b}{\mathrm{d}z} >$	y-shear production

Finally, an evolution equation for the perturbation potential energy (per unit mass) $PE' = -Ri_h < z\theta >$ can be derived by multiplying (4.4) by z and integrating over the domain:

$$\frac{\mathrm{d}PE'}{\mathrm{d}t} = -B + Ri_h \int_{-1}^{0} z\bar{v}\,dz + \frac{Ri_h}{Pe} \int_{-1}^{0} \frac{\partial\bar{\theta}}{\partial z}dz, \tag{4.8}$$

28

where the overbar refers to a y average. Thus, when w and θ are positively correlated, as in Figure 4-1(a), potential energy is released from the background lateral density gradient and converted to cross-front kinetic energy. The second two terms on the right-hand side of (4.8) vanish for *linear* disturbances (v,θ), which necessarily have zero horizontal average; that is, for small-amplitude disturbances, buoyancy production B is the only factor that can alter the perturbation potential energy. In this section, we evaluate $D_{\parallel}$, $D_{\perp}$, B, P_S, P_U, and P_V using the eigenfunctions obtained from the linear stability computations to evaluate the parametric dependencies of these various physical processes. However, it is important to bear in mind that during the *nonlinear* phase of the disturbance evolution, the potential energy may be altered by the last two terms in (4.8). In fact, these physical effects provide important clues for interpreting the dynamics observed in the fully nonlinear numerical simulations. Figures 4-2 and 4-3 show the relative magnitudes of the various terms in the energy budgets, each normalized by

$$\frac{\mathrm{d}KE'_{\perp}}{\mathrm{d}t} = 2\sigma_r\, KE'_{\perp},$$

which holds for linearized dynamics. This normalization indicates the contribution of each energy source or sink to the generation of a unit of "cellular flow" energy in the y–z plane. We consider the free and frozen stratification scenarios in turn.

4.2 $\chi = 1$

The key to interpreting the difference between the energetics (and dynamics) of the free and frozen stratification scenarios is that in the former case ($\chi = 1$), the base state cross-front shear flow $V^b(z)$ creates *stabilizing* vertical stratification $\Theta^b(z)$ that is absent – at least initially – in the latter.

Stationary case

As shown in Figures 4-2, buoyancy production is negative as cross-wind kinetic energy is consumed and converted into potential energy. For the stationary instability mode, cells with an $O(1)$ aspect ratio grow most rapidly. Stokes production and x-shear production by the Reynolds stress $\overline{uw}$ increases $KE'_{\perp}$ and $KE'_{\parallel}$, respectively. However, some of the cross-front perturbation kinetic energy is converted to increased potential energy as the cells, which penetrate the entire depth of the mixed layer, do work against gravity by elevating cold, dense fluid (and conversely). For $0.08 < Ri_h < 0.012$, this energy conversion is the predominant dynamic, eradicating the tendency of the layer to be vertically stratified. As Ri_h is increased in this parameter regime, ever stronger winds and surface waves are required to maintain the LC, since the majority of the extracted energy is converted to potential energy (and downwind kinetic energy). When $Ri_h > 0.012$ dissipation increases dramatically, and the LC is weakened.

Traveling cases

Eventually, as shown in figure 3-7, when $Ri_h \gg O(0.01)$, LC in the stationary mode can not be sustained. Instead, the system then responds by developing traveling wave instabilities, in which narrower cells are generated. The background cross-front shear flow tears the cells apart, and two sets of cells travel with the counter-propagating shear flow in opposite directions (see Figures 3-3b,c). A strong vertical temperature gradient is formed, dividing the domain into two layers with fluid traveling in different directions in each region. In this manner, fluid particles carried around individual cells do not cross regions of large vertical temperature gradients, and, as shown in Figure 4-2(a), buoyancy production, while still negative, does not increase in magnitude as the lateral stratification (i.e. Ri_h) is increased. In this configuration, the system is

able to efficiently generate LC relative to the stationary mode. Figure 4-2(a) suggests that the maximum "efficiency" in this sense is attained when $Ri_h \approx 0.013$. With a further increase of Ri_h, less potential energy is stored but more energy is consumed by viscous dissipation.

4.3 $\chi = 0$

When the lateral stratification is maintained ($\chi = 0$), e.g. by a front in thermal wind balance, purely buoyancy-driven instability is possible. Indeed, when $\chi = 0$, Figures 4-3(a) an 4-3(b) confirm that buoyancy production is strictly positive, in contrast to the $\chi = 1$ scenario described above.

$dU_s/dz = 0$ - buoyancy driven instability

The fastest growing instability in the absence of surface waves takes the form of stationary, counter-rotating convection cells inclined in the direction of increasing density gradient. Figure 4-3(a) suggests that the convection becomes more efficient as Ri_h is increased.

$dU_s/dz = 1$

When the Stokes drift gradient is non-zero, the dominant contribution to the cross-wind perturbation kinetic energy is Stokes production for (physically reasonable) values of $Ri_h < 1.4$. However, the fastest growing mode continues to take the form of stationary, counter-rotating cells inclined in the direction of the lateral density gradient, because these modes also benefit from positive buoyancy production. Again, for typical submesoscale fronts with $Ri_h = O(0.1)$, the purely buoyancy-driven instability is very weak (with growth rates on the order of 1 day or longer), while the cooperative instability that occurs in the presence of both surface waves and the lateral density

gradient is much stronger (with growth rates on the order of tens of minutes).

In both cases, it is important to appreciate that the inclined convection cells tend to drive *vertical* stratification of the mixed layer. This has important ramifications for the nonlinear evolution of the primary instability, as described in the following section.
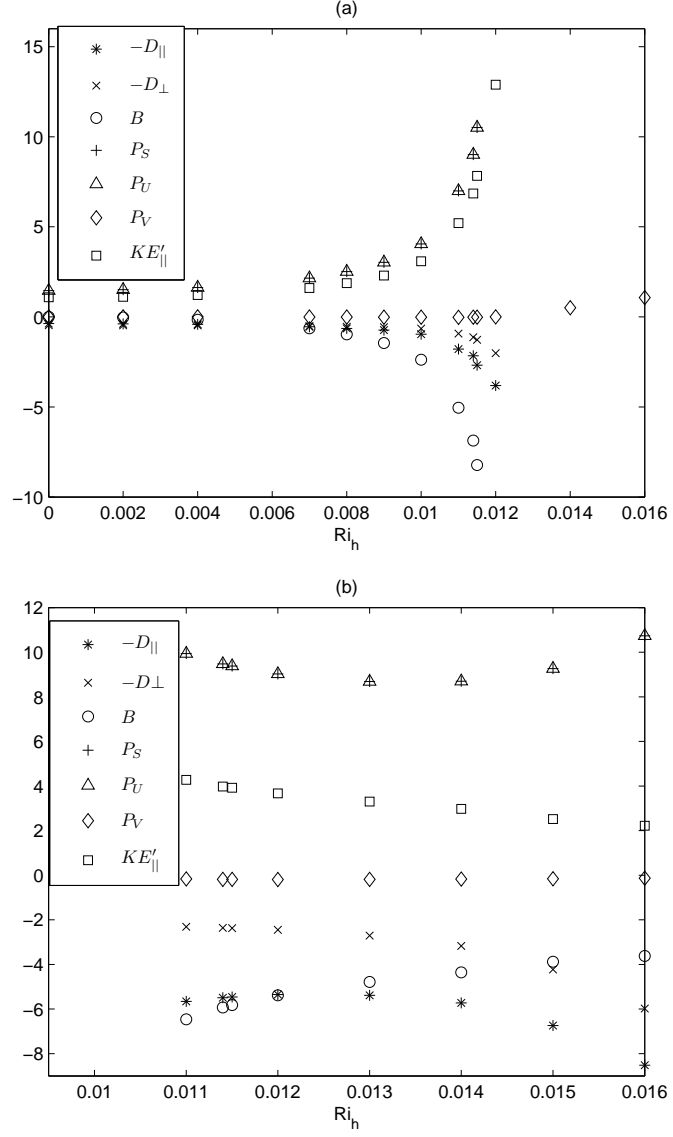
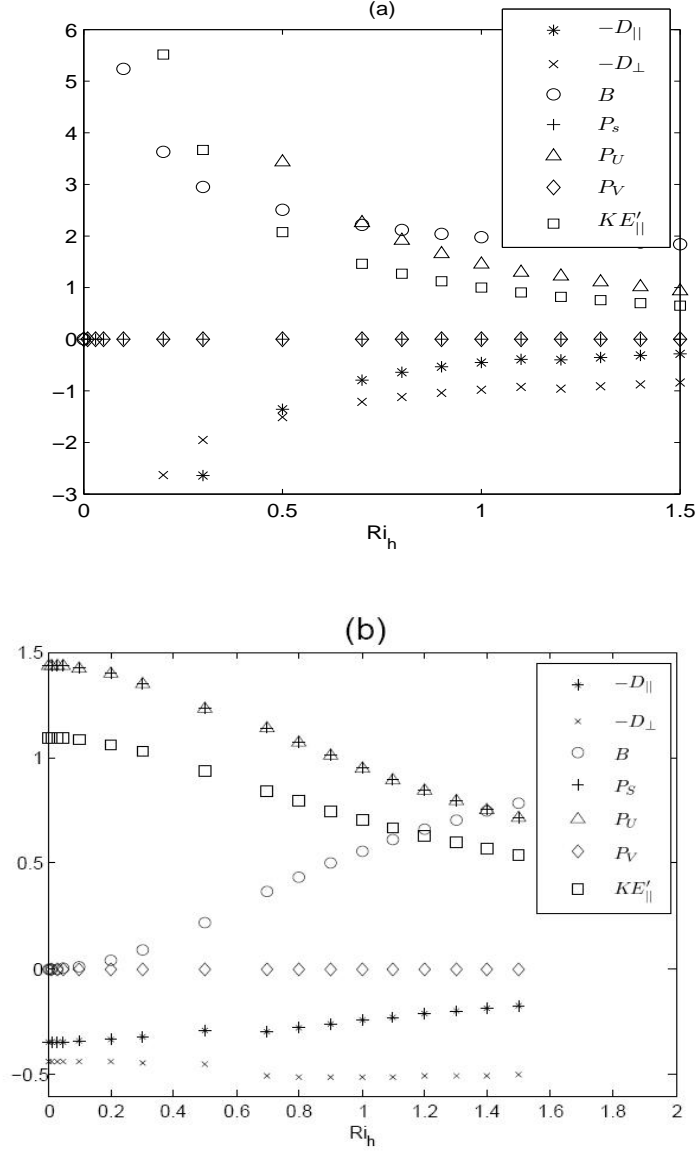Figure 4-2: Energy contributions, $\chi = 1$, $La = 0.01$, and $Pe = 4000$: (a) stationary modes; (b)traveling modes.

Figure 4-3: Energy contributions, $\chi = 0$, $La = 0.01$, and $Pe = 4000$: (a) $dU_s/dz = 0$; (b)$dU_s/dz = 1$.

CHAPTER 5

Direct Numerical Simulations

5.1 Numerical Method

Spectral methods are employed to simulate the system in space, where in the x direction, where blows the wind, nothing varies. Variables vary periodically, crossing $10 \sim 20$ cells in the y direction, and nonperiodically in the z direction. We apply Fourier expansion on y and Chebyshev expansions on z. The dependent variables are first transformed in Fourier series direction using:

$$U(y, z, t) = \sum_{n=-N_y/2+1}^{N_y/2} \hat{U}_n(z, t)e^{inky}, \qquad \Omega(y, z, t) = \sum_{n=-N_y/2+1}^{N_y/2} \hat{\Omega}_n(z, t)e^{inky},$$

$$\Psi(y, z, t) = \sum_{n=-N_y/2+1}^{N_y/2} \hat{\Psi}_n(z, t)e^{inky}, \qquad \Theta(y, z, t) = \sum_{n=-N_y/2+1}^{N_y/2} \hat{\Theta}_n(z, t)e^{inky}, \quad (5.1)$$

where N_y is the number of modes truncated, same as resolution in the physical y domain, n is the mode number, and $k = 2\pi/L$ is the period of cross-wind large box domain. After Fourier transform, we expand $\hat{\Phi}_n$, a generic form of dependent variables, into Chebyshev expansion. The motivation is to solve those four unknown variables with Clenshaw-Curtis algorithm space-wise.

One notices that $z \in (-1, 0)$ in the system, while $Z \in (-1, 1)$ is required for Chebyshev transform. Therefore, one must transform the non dimensional physical domain z in to a new domain Z, and the relation for converting between domains is $Z = 2z + 1$. There is a factor $\xi = 2$ for the converting of derivatives, written as:

$$\frac{\partial(\cdot)}{\partial z} = \frac{\partial(\cdot)}{\partial Z}\frac{\partial Z}{\partial z} = \xi\frac{\partial(\cdot)}{\partial Z} \tag{5.2}$$

Temporal time discretization is performed with semi-implicit form, where linear terms including diffusion takes Crank-Nicolson implicit method and nonlinear terms (such as advection, buoyancy force, and C-L vortex force) takes 2nd-order Adams-Bashforth explicit method. An general equation with a generic variable Φ has been presented marching from time step s and $s-1$ to $s+1$ as

$$\frac{\Phi^{(s+1)} - \Phi^{(s)}}{\Delta t} = \frac{LT^{(s+1)} + LT^{(s)}}{2} + \frac{1}{2}[3NT^{(s)} - NT^{(s-1)}] \qquad (5.3)$$

where LT is abbreviated for linear terms, and NT for nonlinear terms. Apply this temporal discretization to equation, and rearrange the terms at new time step $s+1$ level to the left and the others to the right of the equation, which gives:

$$\hat{U}_{nZZ}^{(s+1)} - \lambda_n \hat{U}_n^{(s+1)} = \gamma_n \hat{U}_n^{(s)} - \hat{U}_{nZZ}^{(s)} - \frac{La^{-1}}{\xi^2}[3F_n^{(s)} - F_n^{(s-1)}], \qquad (5.4)$$

$$\hat{\Omega}_{nZZ}^{(s+1)} - \lambda_n \hat{\Omega}_n^{(s+1)} = \gamma_n \hat{\Omega}_n^{(s)} - \hat{\Omega}_{nZZ}^{(s)} - \frac{La^{-1}}{\xi^2}[3G_n^{(s)} - G_n^{(s-1)}], \qquad (5.5)$$

$$\hat{\Theta}_{nZZ}^{(s+1)} - \Lambda_n \hat{\Theta}_n^{(s+1)} = \Gamma_n \hat{\Theta}_n^{(s)} - \hat{\Theta}_{nZZ}^{(s)} - \frac{Pe}{\xi^2}[3H_n^{(s)} - H_n^{(s-1)}], \qquad (5.6)$$

$$\hat{\psi}_{nZZ}^{(s+1)} - \eta_n \hat{\psi}_n^{(s+1)} = \frac{\hat{\Omega}_n^{(s+1)}}{\xi^2}, \qquad (5.7)$$

where,

$$\lambda_n \equiv [\eta_n + \frac{2}{\xi^2 \Delta t La}], \qquad \Lambda_n \equiv [\eta_n + \frac{2Pe}{\xi^2 \Delta t}], \qquad (5.8)$$

$$\gamma_n \equiv [\eta_n - (\frac{2}{\xi^2 \Delta t La})], \qquad \Gamma_n \equiv [\eta_n - (\frac{2Pe}{\xi^2 \Delta t})] \qquad (5.9)$$

$$\eta_n \equiv \frac{(nk)^2}{\xi^2}; \qquad (5.10)$$

$$F_n \equiv \xi(\widehat{\psi_y u_z - \psi_z u_y}), \qquad (5.11)$$

$$H_n \equiv \xi(\widehat{\psi_y \Theta_z - \psi_y \Theta_y}); \qquad (5.12)$$

$$G_n \equiv \xi(\widehat{\psi_y \Omega_Z - \psi_z \Omega_y + \frac{dU_s}{dZ} u_y}); \qquad (5.13)$$

Equations - are in the basic diecretized form called Helmholtz equation, where $s+1$ is unknown time step, $\Phi_n^{(s+1)}$ is the dependant variable with respect to Z. In order to solve for variables at $s+1$ time step, Clenshaw-Curtis Algorithm is employed.

A Fourier–Chebyshev-tau pseudospectral algorithm developed in-house was used to numerically integrate the governing non-hydrostatic, laterally stratified, x-invariant (i.e. 2D, 3-component) CL equations (2.3)–(2.6) for both $\chi = 0$ and for a range of initial data. Each dependent variable was expanded in Fourier modes in the y coordinate and Chebyshev polynomials in z. A semi-implicit time stepping method was employed, with the diffusive terms advanced using the Crank–Nicholson scheme and the linear cross-coupling and nonlinear advection terms advanced with an explicit second-order Adams–Bashforth formula. The discretized form of governing equations can be written as:

$$\frac{U^{(s+1)} - U^{(s)}}{\Delta t} = \frac{LT^{(s+1)} + LT^{(s)}}{2} + \frac{1}{2}[3NT^{(s)} - NT^{(s-1)}] \qquad (5.14)$$

where U stands for variables in the equations and LT and NT represent linear terms and nonlinear terms. The resulting Helmholtz equation (in z) is solved using the Clenshaw–Curtis algorithm (using a fast Chebyshev transform) in $O(\mathcal{M})$ operations per horizontal wavenumber, where $\mathcal{M} + 1$ is number of Chebyshev modes.

We explore the DNS from three categories, the homogeneous case, the free case, and the frozen case. As a brief introduction of DNS, here gives the computation software and compiler. The software includes: fftw-3.1.2. Fortran 99 installed on a linux based system.

5.2 $\chi = 0$

Of primary interest for the DNS is the scenario in which the background lateral stratification is maintained without a cross-front shear flow (i.e. $\chi = 0$). The results for this case are shown in Figures 5-2–5-4. In each of the simulations, $La = 0.01$,
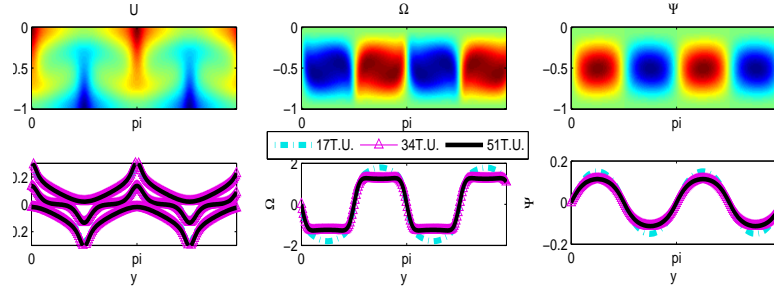
Figure 5-1: DNS result, homogeneous case, with $La = 0.01$, $Pe = 4000$

$Pe = 4000$, and $\mathrm{d}U_s/\mathrm{d}z = 1$.

Parameters			
N_y	650	N_z	128
χ	0.0	Δt	0.001
Pe	4000	Ri_h	4.0
La	0.01	dU_s/dz	1.0
I.C.			
perturb with $k = 4.4$			
perturb with $k = 4.0$, 4.4, and 4.8			
homogeneous case			

The former parameter choices were dictated by balancing the need for suppressing the direct influence of dissipative effects and obtaining numerically stable simulations with modest spatiotemporal resolution. The width of the computational domain was varied between approximately 4 (small aspect ratio) and 16 (large aspect ratio). For

Figure 5-2: DNS result, frozen case with $La = 0.01$, $Pe = 4000$, and $Ri_h = 4.0$. It starts from an small-amplitude sinusoid initial condition of which the horizontal wave number $k = 4.4$, in the line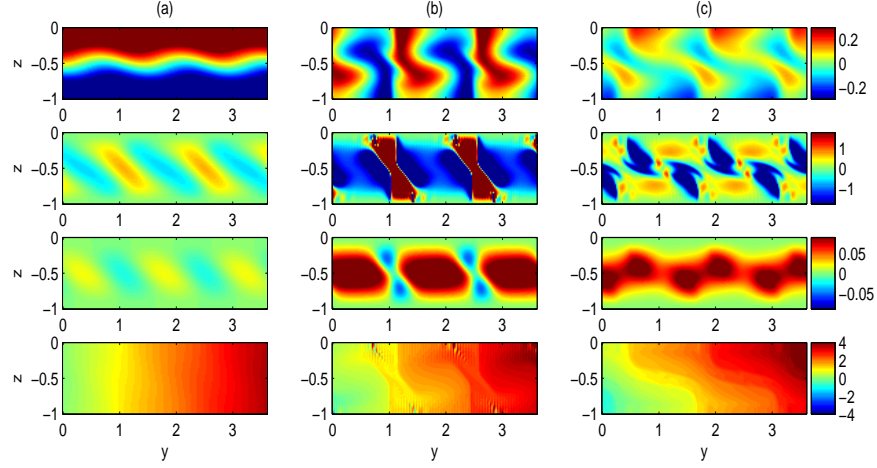ar theory, gives the maximum growth rate. It can be represented by 3 phenomenal time steps, where for each graph set, the variables plotted are U, Ω, Ψ, T from top to the bottom: (a) 52 T.U.; (b) 87 T.U.; (c) 108 T.U.

reference, the results of the homogeneous case $(Ri_h = 0)$ are displayed in Figure 5-1.

Parameters			
N_y	512	N_z	64
χ	0.0	Δt	0.001
Pe	4000	Ri_h	0.0
La	0.01	dU_s/dz	1.0

As is evident in this figure, for the given parameter values, a range of initial conditions eventually saturate in the form of fully nonlinear but steady Langmuir cells with homogenized vortex cores.

To highlight the effects of imposed lateral stratification on LC, we set $Ri_h = 4.0$ (an admittedly large value). Figure 5-2 shows the evolution of the various fields starting
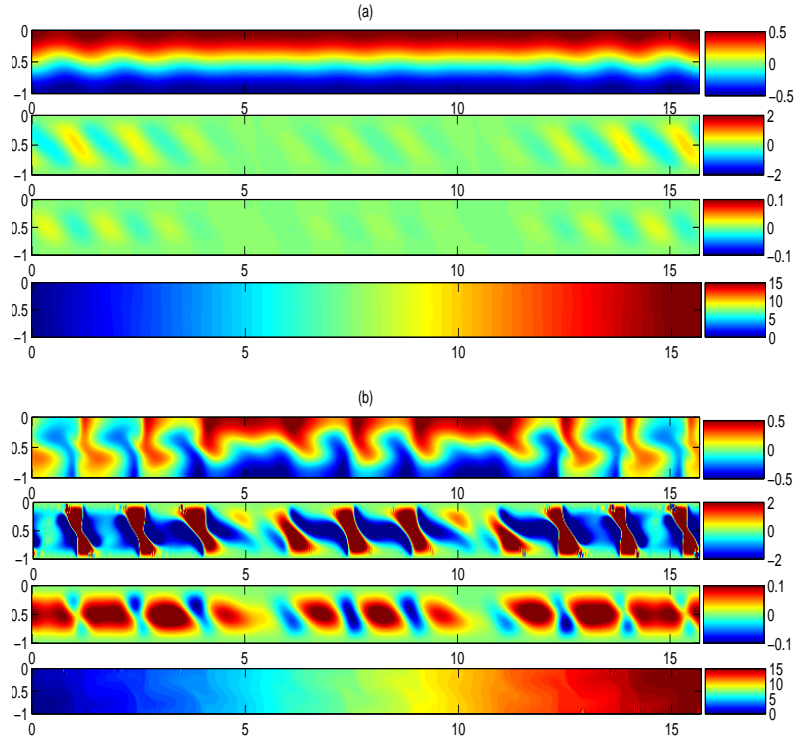
from a small-amplitude initial disturbance consisting of a single Fourier mode in the y direction with wavenumber $k = 4.4$, which is predicted to be the fastest growing mode according to linear theory (see Figure 3-4), superimposed on $U^b(z) = z + 1$. In accord with linear theory, this mode rapidly intensifies (within the first few non-dimensional time units, not shown in the figure). Within the first 3 time units, upwelling and downwelling jets between cell pairs become inclined to the vertical in the direction of increasing density. By $t = 5.2$ (the left-hand plot in Figure 5-2), an asymmetry in the convective pattern is first manifest. When $t = 8.7$ (middle plot), this asymmetry becomes distinct: the cells with positive x vorticity (Ω, the *negative* x vorticity is plotted in the second row) are much stronger and wider than the oppositely-rotating cells, which begin to shear apart. The fully nonlinear simulations reveal that the convective pattern undergoes a *secondary* instability, with the sheared cells propagating in the direction of the density gradient near the top of the mixed layer and

40
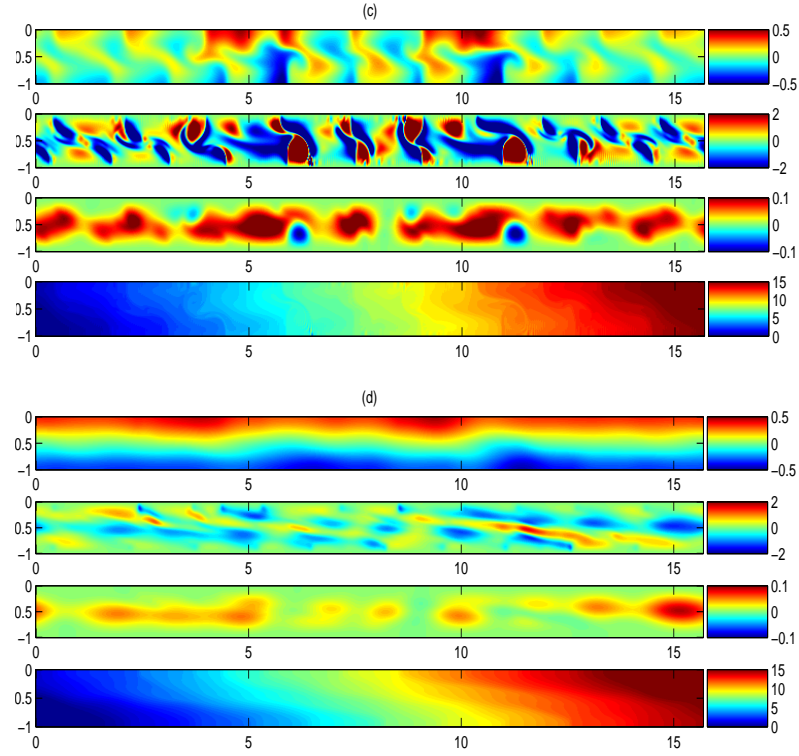
Figure 5-3: DNS result, frozen case with $La = 0.01$, $Pe = 4000$, $Ri_h = 4.0$. The initial condition is the fastest growing mode when $k = 4.4$ together with two other modes in vicinity at each side where, $k = 4.0$ and $k = 4.8$ respectively. It can be represented by 4 phenomenal time steps, where for each graph set, the variables plotted are U, Ω, Ψ, T from top to the bottom: (a)3.8 T.U.; (b) 7.8 T.U.; (c) 9.9 T.U.; (d) 17.8 T.U.

oppositely near the base of the layer. For the chosen parameters, this dynamic is roughly time periodic and resembles a "stick-slip" phenomenon, a snapshot of which is shown in the right-hand plot of Figure 5-2. However, the behavior is not purely periodic, and in each "cycle," increasingly fine vertical structure is created, with energy ultimately cascading to finer scales. The cellular asymmetry that precipitates the onset of the secondary instability suggests that nonlinear "self–self" interactions of the primary instability mode favor cross-front flows with positive x vorticity. Cru-

(a)

(b)

y

(c)

y
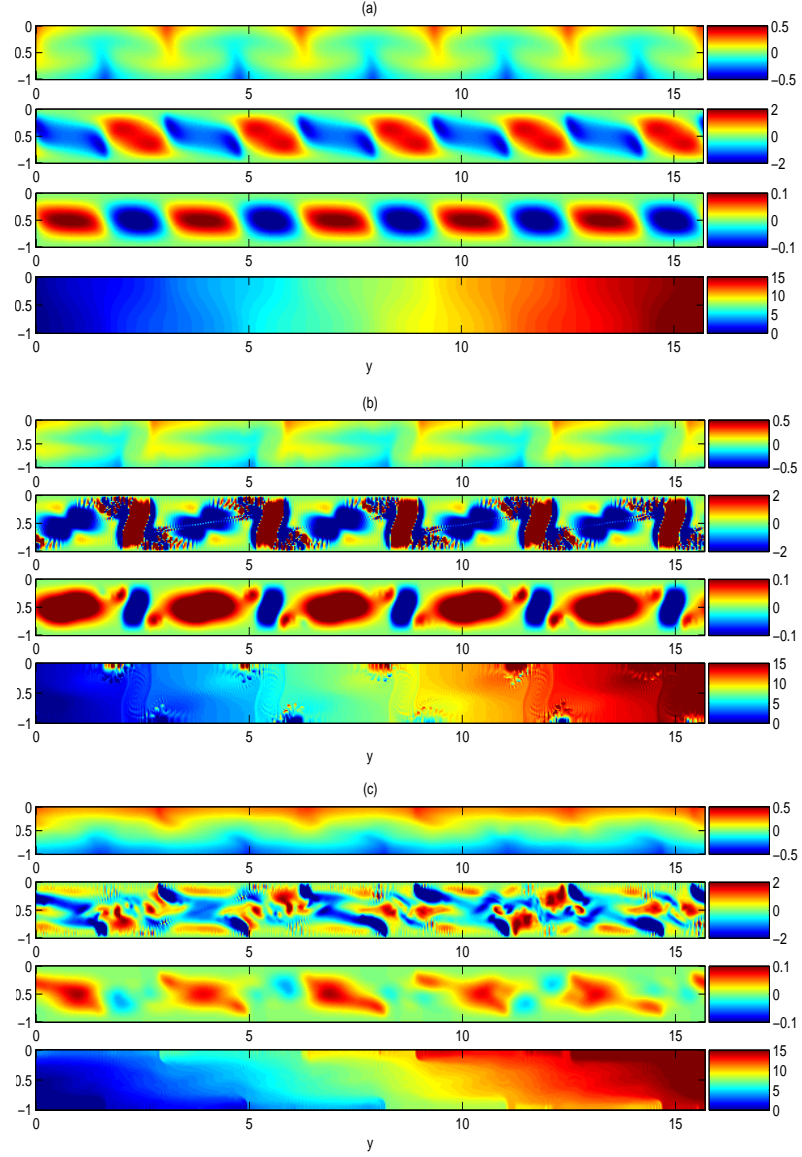
cially, we observe that the net effect is very similar to advection of the background density gradient by $V^b(z)$ in the free ($\chi = 1$) scenario: lighter fluid is advected over heavier, creating a stabilizing *vertical* stratification that favors counter-propagating disturbances confined to the upper and lower parts of the mixed layer, respectively (cf. the traveling wave modes in Figure 5-2 and 5-3 and the discussion of their energetics in the previous section). In Figures 5-3 and 5-4, broadly similar behavior is observed, both for initial data comprised of the fastest growing primary mode with

42

even smaller amplitude sideband modes (Figure 5-3) and for initial data consisting of the fully equilibrated Langmuir cells shown in Figure 5-2 (Figure 5-4). Thus, for a broad range of initial conditions, the phenomenology consisting of linear instability to tilted cells, asymmetrization of the cells, and secondary instability involving cell shearing and counter-propagating disturbances is observed to occur over $O(10)$ time units; this corresponds to about 5-10 hours. In each case, the long time effect is to *vertically* stratify the mixed layer over this time scale.

Numerical simulations on a relatively small Ri_h is performed to verify the case when horizontal shear flow is comparably weaker than the vertical convection drawn by Langmuir circulations. According to the energy budget results Figure 4-3b, when $Ri_h = O(0.1)$, Stokes drift and Reynold's stress provide more energy than the vertical buoyancy term, which to the extreme becomes homogeneous case when $Ri_h \to 0$. In the extreme case $Ri_h \to 0$, only Stokes drift due to the surface wave and along wind shear flow convert energy to the cross-wind cellular flow. Here $Ri_h = 0.5$ is picked in the simulation, together with other parameters listed as:

Parameters			
N_y	650	N_z	64
χ	0.0	Δt	0.001
Pe	4000	Ri_h	0.5
La	0.01	dU_s/dz	1.0

where instability is alternating on and off periodically in the secondary instability as shown in Figure 6. The cells in the middle of the domain are torn apart when they are weakened. "Stick slip" phenomenon takes place. Most interestingly, the subcells torn part from the middle travel up the lateral gradient. Traveling cells bring cold fluid up gradient on the top and warm fluid down gradient at the bottom, preventing the isopycnal from being tilted by the thermal convection. Both thermal convection

and Langmuir circulation happen together, causing the temperature is distributed in the shape of stair case. If one focuses on the temperature profile, it is well maintained all through the way and vertical cellular flows are "locked" in the certain region. It is strong enough to prevent the isopycnal from tilting toward horizontal.

Simulations for comparison is also done, in which Stokes drift is turned off. The system is driven by purely vertical thermal convection. In this case, along wind direction is decoupled from the across-wind domain where vertical convection still exists.

Parameters			
N_y	650	N_z	64
χ	0.0	Δt	0.001
Pe	4000	Ri_h	0.5
La	0.01	dU_s/dz	0.0

Figure 5-6 shows the pure thermal convection driven flow shows a restratified vertical temperature gradient start to shear the cellular flow apart and cells on top travel down the gradient and bottom up the gradient so that hot fluid will sit on top of cold. It directly performs the vertical buoyancy driven convection. From figure 4-3a, case with big Ri_h corresponds with a more efficient instability than one with small Ri_h. In another words, the instability of $Ri_h = 0.5$ tends to be weaker compared with cases of bigger Ri_h, with restratification to be longer than $Ri_h = 4.0$. This conclusion can be verified by the DNS results Figure 5-6c. Moreover, by comparing the two cases, one can be convinced that Langmuir circulation helps on maintaining the isopycnal to the vertical. Under the most commonly seen value $Ri_h = 0.5 = O(0.1)$, Langmuir circulation greatly enhanced the vertical convection and plays a role connecting the deep ocean to the surface.

5.3 $\chi = 1$

Finally, DNS for the free cases ($\chi = 1$) is shown in Figures 5-7(a) and (b,c).

Parameters			
N_y	650	N_z	64
χ	1.0	Δt	0.001
Pe	4000	Ri_h	0.016
La	0.01	dU_s/dz	1.0
I.C.			
perturb with $k = 3.75$			

Parameters			
N_y	650	N_z	128
χ	1.0	Δt	0.001
Pe	4000	Ri_h	0.01
La	0.01	dU_s/dz	1.0
I.C.			
perturb with $k = 2.55$			

For the smaller k instability mode (wider cells), the bifurcation is stationary and LC preserves lateral stratification but mixes vertical stratification, creating a horizontal staircase pattern in the temperature field. For the larger k instability mode (narrow cells), the bifurcation involves cell shearing reminiscent of the secondary instability in the frozen case.
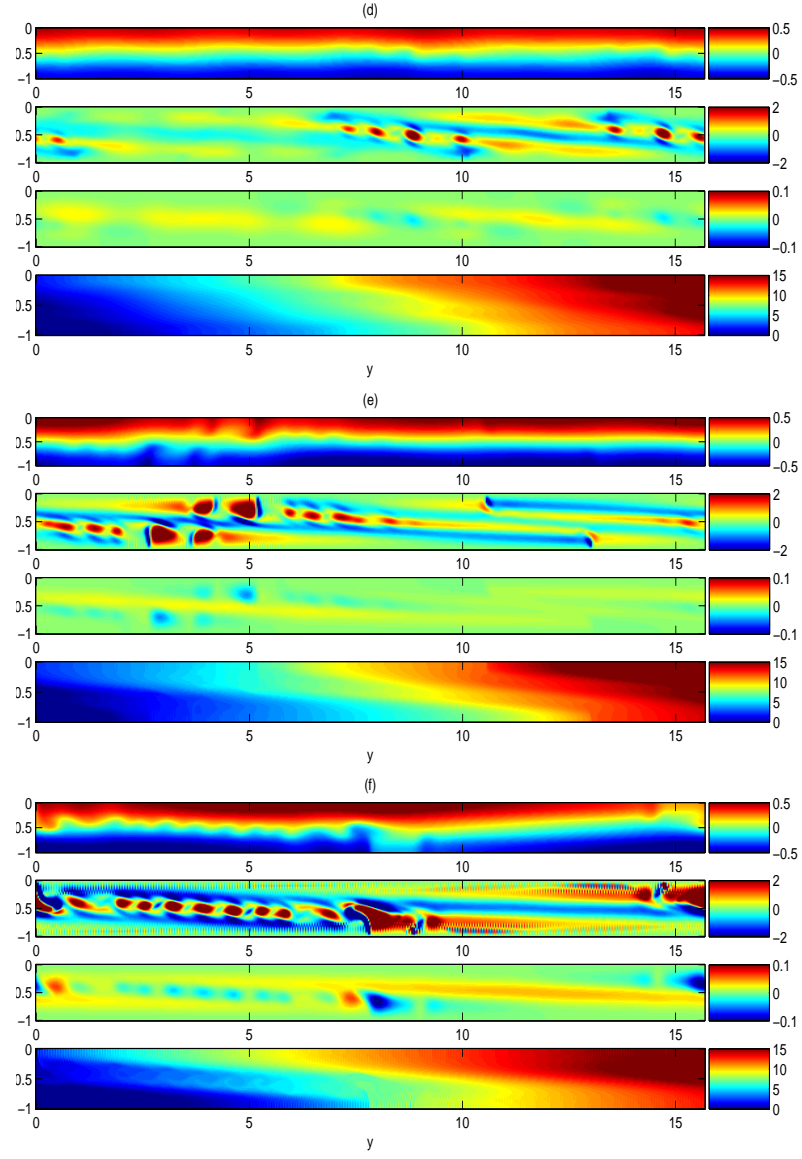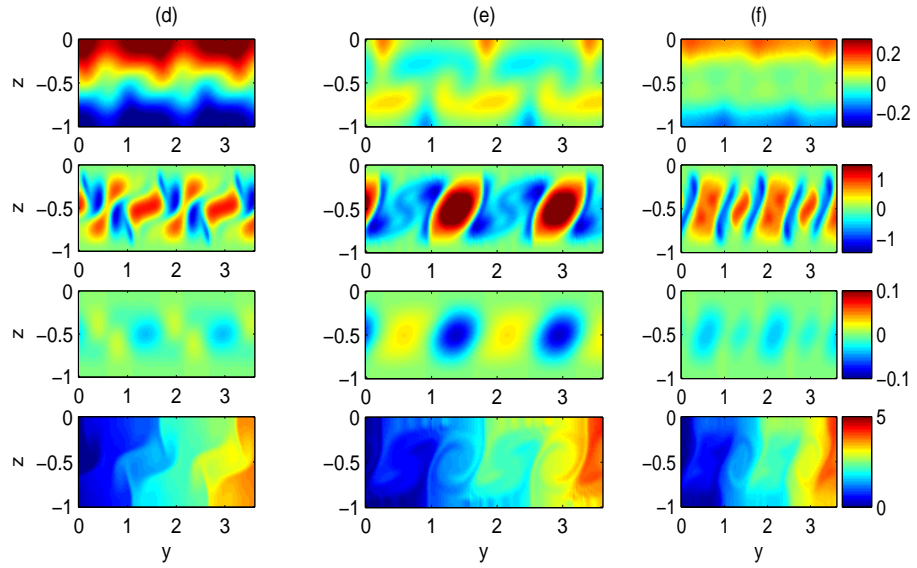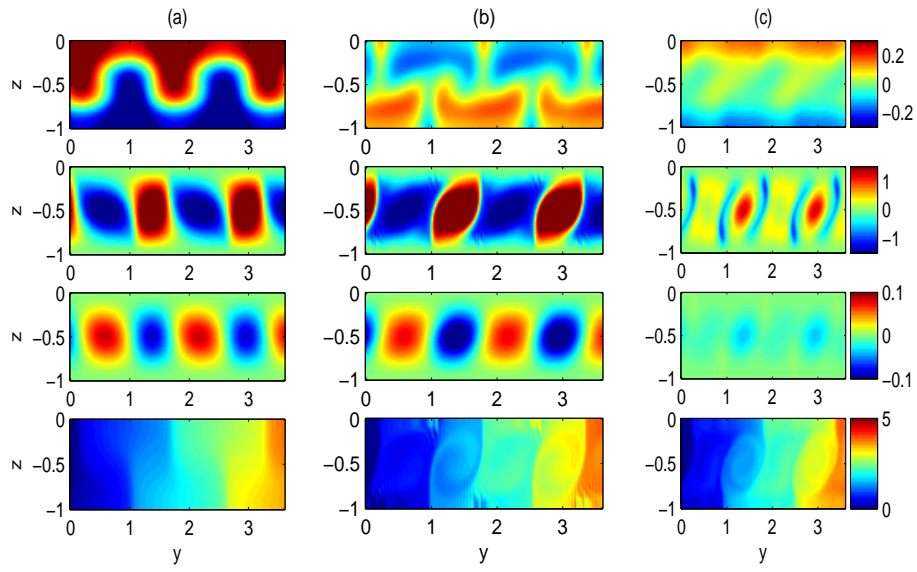
Figure 5-4: DNS result, frozen case with $La = 0.01$, $Pe = 4000$, $Ri_h = 4.0$. The initial condition is Fig(5-1). It can be represented by 5 phenomenal time steps, where for each graph set, the variables plotted are U, Ω, Ψ, T from top to the bottom: (a)1.2 T.U.; (b) 3.8 T.U.; (c) 8.6 T.U.; (d) 20 T.U. (e)61.5 T.U.; (f)208 T.U.

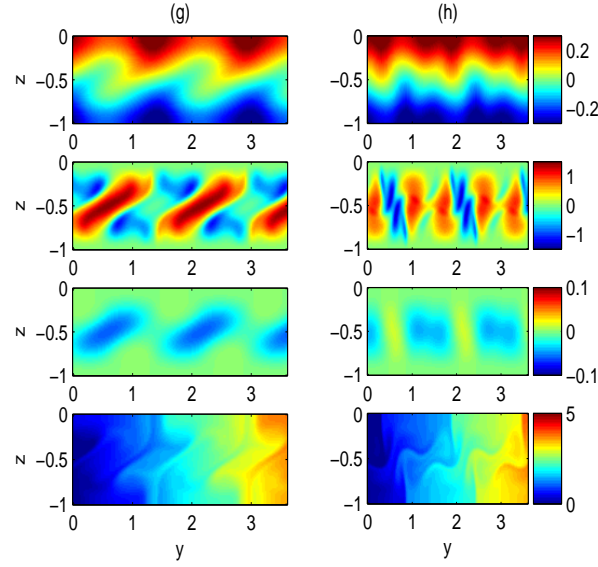Figure 5-5: DNS result of frozen case with Stokes drift in different time steps: (a) 8.4 T.U.; (b) 11.5 T.U.; (c) 14.8 T.U.; (d) 22.6 T.U.; (e) 29.3 T.U.; (f) 31.7 T.U.; (g) 36.6 T.U.; (h) 55.8 T.U. The variables plotted are U, Ω, Ψ, T from top to the bottom. Parameters are displayed as: $Ny = 650$, $Nz = 64$, $\chi = 0.0$, $\Delta t = 0.001$, $Pe = 4000$, $Ri_h = 0.5$, $La = 0.01$, and $dU_s/dz = 1.0$
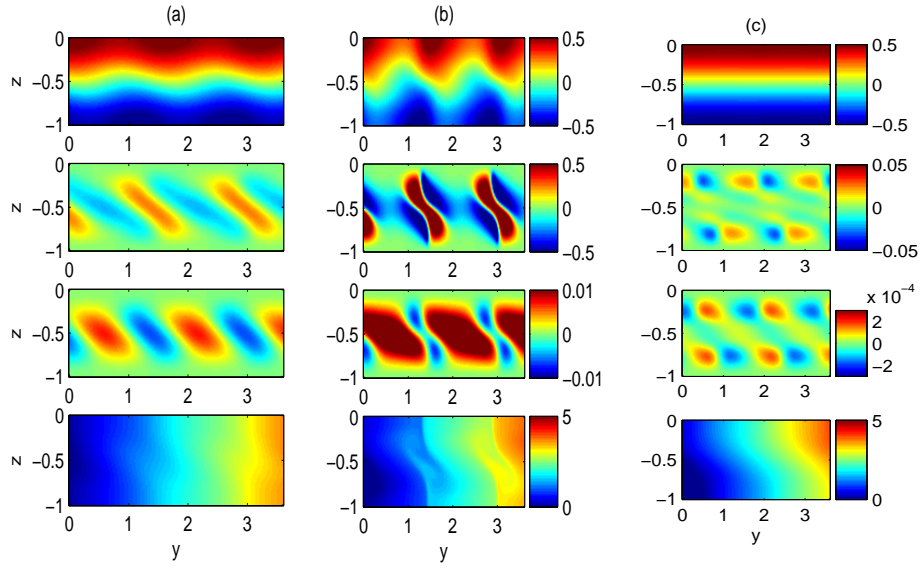
Figure 5-6: DNS result of frozen case without Stokes drift in different time steps: (a) 12.5 T.U.; (b) 27.7 T.U.; (c) 120 T.U. The variables plotted are U, Ω, Ψ, T from top to the bottom. Parameters are displayed as: $Ny = 650$, $Nz = 64$, $\chi = 0.0$, $\Delta t = 0.001$, $Pe = 4000$, $Ri_h = 0.5$, $La = 0.01$, and $dU_s/dz = 0.0$

Figure 5-7: DNS result, the variables plotted are U, Ω, Ψ, T from top to the bottom:(a) stationary $k = 2.55$, $Ri_h = 0.01$, $La = 0.01$, $U'_s(z) = 1$, and $Pe = 4000$ at 60.1 T.U.; (b & c) Traveling mode $k = 3.75$, $Ri_h = 0.016$, $La = 0.01$, $U'_s(z) = 1$, and $Pe = 4000$ (b) 37.7 T.U.; (c) 75.4 T.U.

CHAPTER 6

Conclusions and Future Work

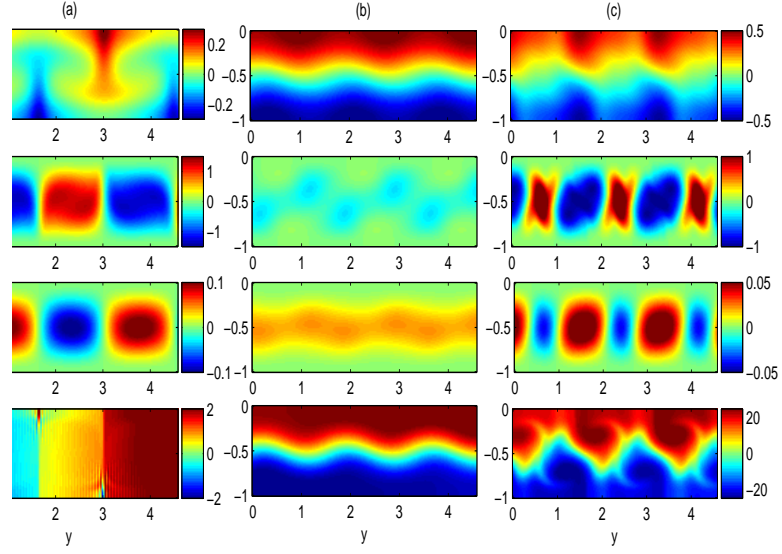Langmuir circulation is a primary vertical mixing process driven by the wind and surface waves. In this paper it is imposed into a horizontal temperature gradient associated with submesoscale front. It includes two big categories regarding the backgrounds.

The first one has a background with a maintained horizontal temperature gradient. It tends to describe a lateral stratification in the ocean's mixed layer maintained by large scale oceanography dynamics. In the absence of Langmuir circulation, a buoyancy driven convection takes place. The isopycnal lines are slanted from the vertical due to the gravity. It by itself is able to reach a steady state. With Langmuir circulation added on the background, it mixes with the vertical stratification within the mixed layer depth.

The other one has a background with horizontal shear flow driven by the temperature gradient. The lateral temperature gradient drives the horizontal shear flow balanced by the vertical molecular diffusion. If Langmuir circulation is strong enough compared with horizontal shear flow at the background, the shear flow is blocked, Langmuir cells tend to mix the vertical temperature gradient and horizontal gradient. In this case, Langmuir cells would stay stationary. If Langmuir circulations are weak, horizontal shear flow tends to shear cells apart and takes sub-cells traveling with the flow, which is called traveling case.

Craik-Leibovich model is employed with the vortex forcing term added. The

vortex forcing transports energy from the wind on the x direction to the cellular flow on the y-z domain, revealing the surface wave connecting the surface wind to the cross-wind turbulence. To this extent, this model shares some mathematical features with symmetric instability in the mesoscale ocean, which connects the instability across the mesoscale front to the third dimension along the front through thermal wind.

A pseudo-spectral numerical method has been developed in Fortran 90 to simulate this interesting phenomenon. Linear stability analysis has been performed to reveal the physical insight of Langmuir circulation. It provides the growth rate distribution associated with horizontal cell sizes. Traveling and stationary modes are distinguished from this analysis. In this method, fast Fourier transform is only utilized on the horizontal direction, with vertical discretized in Chebyshev transform. Chebyshev Spectral Collocation Method was the algorithm to numerically calculate the eigenvalue problem. Moreover, another analytical linear stability analysis is invented to associate the tilting angle of cells to the physical parameters. It is a simple basic model with the advantage of easy performing. In this method, fast Fourier transform is applied on both vertical and horizontal directions.

Energy budget reveals the spin-up energy distribution of the linearized system. It lines up with the simulation results that in frozen case, Langmuir circulation and buoyancy convection assist each other during the spin-up scale as the first order but work against each other after the vertical restratification as a higher order phenomenon. A weak lateral density gradient such as $Ri_h \sim O(1)$, as a matter of fact from DNS, is associates with a horizontal entrainment to the upstream in a way to maintain the vertical mixing, which can be shown in Figure

As part of the future work, appropriate parameterizations such as smaller La and $Ri_h \approx O(0.1)$ are desirable. Secondary instability analysis needs to be performed to

illustrate the secondary linearized behavior based on the solutions of the first-order linear stability analysis. Galerkin projection methods can be used for solving multiple linear system. One should analyze the energetic budget for numerical simulation in order to approach the secondary instability. Compared with the first order energetic budget, the secondary one gives energy transport involving terms that are cut off due to linearization but not necessarily small. Charts with energetic developing with time are desired to give a clear view of energy transport between the Langmuir circulations and the lateral density gradient. Adding Coriolis parameters creating lateral density gradient by Thermal Wind balance serves to embed Langmuir circulation into a real ocean that is governed by the Coriolis force, which is able to produce a horizontal front for Langmuir cells. Interactions between symmetric, baroclinic, and Langmuir circulation instabilities are highly desired.

Bibliography

[Taylor and Ferrari 2010] Taylor, J. and Ferrari, R. 2010. *Buoyancy and wind-driven convection at a mixed-layer density fronts.* J. Phys. Oceanogr., Vol. 40, 1222-1242

[McWilliams et al 1997] McWilliams, J.C., Ullivan, P.P., and Moeng, C. 1997. *Langmuir turbulence in the ocean.* J. Fluid Mech. 334, 1-30

[Thorpe 2004] Thorpe, S. A. 2004. *Langmuir Circulation.* Annu. Rev. Fluid Mech. 36. 55-79

[Leibovich 1977a] Leibovich, S. 1977a. *Convective instability of stably stratified water in the ocean.* J. Fluid Mech. 92, 561-585

[Leibovich 1977b] Leibovich, S. 1977b. *On the evolution of the system of wind drift currents and Langmuir circulations in the ocean. Part 1. Theory and averaged current.* J. Fluid Mech. 79, 715-743

[Leibovich 1983] Leibovich, S. 1983. *The form and dynamics of Langmuir circulations.* Ann. Rev. Fluid Mech. 15, 391-427

[Haine and Marshall 1998] Haine, T., and Marshall, J., 1998. *Gravitational, symmetric and baroclinic instability of the ocean mixed layer.* J. Phys. Oceanogr.,28, 634 - 658

[Tandon and Garrett 1995] Tandon, Amit and Garrett, Chris 1995. *Geostrophic adjustment and restratification of a mixed layer with horizontal gradients above a stratified layer.* J. Phys. Oceanogr., 25, 2229-2241

[Thomas 2005] Thomas, L. N. 2005. *Destruction of potential vorticity by winds.* J. Phys. Ocean., 35, 2457-2466

[Boccaletti et al 2007] Boccaletti G., R. Ferrari, and B. Fox-Kemper, 2007. *Mixed Layer Instabilities and Restratification.* J. Phys. Oceanogr., Vol. 37, 2228-2250

[Li and Garrett 1993] Li, M. and C. Garrett. 1993. *Cell merging and the jet/downwelling ratio in Langmuir circulation.* J. Mar. Res., 51, 737-769.